European Journal of Medicinal Chemistry 265 (2024) 116078

Contents lists available at ScienceDirect

European Journal of Medicinal Chemistry

journal homepage: www.elsevier.com/locate/ejmech

Research paper

Targeted liposomes encapsulated iridium(III) compound greatly enhance anticancer efficacy and induce cell death via ferroptosis on HepG2 cells

Jing Chen [a,1], Wenlong Li [a,1], Gechang Li [a], Xiaoming Liu [b], Chunxia Huang [a], Hua Nie [b,**], Lijuan Liang [a], Yi Wang [a], Yunjun Liu [a,*]

[a] School of Pharmacy, Guangdong Pharmaceutical University, Guangzhou, 510006, PR China
[b] Jiaying University, Meizhou, 514031, PR China

ARTICLE INFO

Keywords:
Iridium(III) complex
Targeted liposome
RNA-Sequence
Ferroptosis
Anti-tumor in vivo

ABSTRACT

In this study, ligands 2-phenyl-1H-imidazo[4,5-f][1,10]phenanthroline (PIP), 2-(2-nitrophenyl)-1H-imidazo[4,5-f][1,10]phenanthroline (NPIP), 2-(2-nitronaphthalen-1-yl)-1H-imidazo[4,5-f][1,10]phenanthroline (NNIP) and their iridium(III) metal compounds $[Ir(ppy)_2(PIP)](PF_6)$ (ppy = 2-phenylpyridine, 1a), $[Ir(ppy)_2(NPIP)](PF_6)$ (1b), $[Ir(ppy)_2(NNIP)](PF_6)$ (1c) were designed and synthesized. The anti-cancer activities of 1a, 1b and 1c on BEL-7402, HepG2, SK-Hep1 and non-cancer LO2 were detected using MTT method. 1a shows moderate, 1b and 1c display low or no anti-cancer activities. To elevate the anti-cancer effectiveness, encapsulating the compounds 1a, 1b and 1c into the ordinary or targeted liposomes to produce 1alip, 1blip, 1clip, or targeted 1aTlip, 1bTlip and 1cTlip. The IC_{50} values of 1alip, 1blip, 1clip, 1aTlip, 1bTlip and 1cTlip against HepG2 cells are 7.9 ± 0.1, 8.6 ± 0.2, 16.9 ± 0.5, 5.9 ± 0.2, 7.3 ± 0.1 and 9.7 ± 0.7 μM, respectively. Specifically, the anti-tumor activity assays in vivo found that the inhibitory rates are 23.24 % for 1a, 61.27 % for 1alip, 76.06 % for 1aTlip. It is obvious that the targeted liposomes entrapped iridium(III) compound greatly enhance anti-cancer efficacy. Additionally, 1alip, 1blip and 1clip or targeted 1aTlip, 1bTlip and 1cTlip can effectively restrain the cell colony and proliferation in the G0/G1 period. 1alip, 1blip, 1clip, 1aTlip, 1bTlip and 1cTlip can increase reactive oxygen species (ROS) concentration, arouse a decline in the mitochondrial membrane potential and promote Ca^{2+} release. RNA-sequence was applied to examine the signaling pathways. Taken together, the liposomes or targeted liposomes encapsulated compounds trigger cell death by way of apoptosis, autophagy, ferroptosis, disruption of mitochondrial function and PI3K/AKT/mTOR signaling pathways.

1. Introduction

The serious side-effects of cisplatin stimulate scientist to search other metal compounds as an alternative of cisplatin. As potent anti-cancer reagents, iridium(III) compounds target the mitochondria, proteins, DNA, and lysosomes [1,2]. At present, there are two types of iridium(III) anti-cancer compounds, namely, cyclic metal structures, and semi-sandwich structures [3]. These iridium(III) compounds exert anti-cancer effects via various mechanisms such as inhibiting protein function and catalyzing cellular oxidation [4]. In the past decade, anti-cancer activities of iridium(III) compounds have aroused great interest and found a lot of iridium(III) compounds with distinctive anti-cancer efficacy [5–20]. Zhong et al. reported that iridium compounds can intensify the effects of photodynamic treatment by upsetting the cellular redox equilibrium [21]. Sun et al. found that sulfur-ligated organo-iridium(III) compounds could inhibit tumorigenesis and metastasis in breast cancer by targeting the Wnt/β-catenin signaling pathway [22]. Yi and co-workers discovered $[Ir(ppy)_2(BD-PIP)]PF_6$ triggering A549 cell death through activating PI3K/Akt/mTOR pathway [23].

Recently, because of its non-apoptotic form of controlled cell death, ferroptosis has emerged as a potential target for cancer treatment [24]. Wang et al. discovered that iridium(III) compounds bearing ferrocene alteration relocate to the lysosome and dramatically impact ferroptosis and cancer immunity pathways [25]. On the other hand, liposomes as nano-drugs carriers are widely applied in drug delivery system, and the

* Corresponding author.
** Corresponding author.
E-mail addresses: niehua@jyu.edu.cn (H. Nie), lyjche@gdpu.edu.cn (Y. Liu).
[1] These authors contribute equally.

https://doi.org/10.1016/j.ejmech.2023.116078
Received 18 July 2023; Received in revised form 1 December 2023; Accepted 18 December 2023
Available online 19 December 2023

liposomes are made up of a bilayer structure constructed by phospholipids and cholesterol, the structures of liposome are similar to the biofilm, therefore, all water-soluble and lipid-soluble drugs can be encapsulated into the liposome. In the latest studies, numerous compounds show low or no cytotoxicity, after these compounds have been encapsulated in liposomes, the liposome entrapped compounds display high cytotoxic activity in vitro and vivo [26–28]. Gu et al. reported that the anti-cancer activity of liposome-loaded compound [Ir(Hppy)$_2$(HMNPIP)](PF$_6$) increased by 43.5 times than the compound alone [29].

As expectation, targeted liposome entrapped compounds will show higher anti-cancer efficacy than ordinary (non-targeted) liposomes. The desialic acid glycoprotein receptor (ASGP-R) is an endocytic receptor specifically expressed mainly on the surface of mammalian hepatocytes, while it is rarely found in the non-hepatocytes, and its high binding affinity with molecules such as N-acetylgalactosamine (GalNAc) or galactose or polymers makes it an ideal target for the therapy of hepatocellular carcinoma [30–32]. A breakthrough in the targeted delivery of compounds has been achieved by using GalNAc as a target head to target hepatocellular carcinoma [33]. In order to gain more insights, furtherly understanding the anti-cancer mechanism of iridium(III) compounds, in this article, 2-phenyl-1H-imidazo [4,5-f][1,10[phenanthroline (PIP), 2-(2-nitrophenyl)-1H-imidazo [4,5-f] [1,10]phenanthroline (NPIP) and 2-(2-nitronaphthalen-1-yl)-1H-imidazo [4,5-f] [1,10]phenanthroline (NNIP) were prepared (Scheme 1). Iridium(III) compounds [Ir(ppy)$_2$(PIP)](PF$_6$) (1a), [Ir(ppy)$_2$(NPIP)](PF$_6$) (1b) and [Ir(ppy)$_2$(NNIP)](PF$_6$) (1c) (ppy = 2-phenylpyridine) were successfully synthesized and characterized. The compounds were loaded into the ordinary or targeted liposomes to produce 1alip, 1blip, 1clip or targeted 1aTlip, 1bTlip, 1cTlip. 3-(4,5-dimethylthiazole-2-yl)-2,5-diphenyltetrazolium bromide (MTT) assay showed that 1a showed moderate, 1b and 1c displayed low or no effect on blocking the proliferation of BEL-7402, HepG2 and SK-Hep1, while 1alip, 1blip, 1clip or 1aTlip, 1bTlip and 1cTlip exerted excellent anti-cancer activity.

2. Results and discussion

2.1. Chemistry

The absorption and luminescence spectra of 10.0 μM compounds 1a, 1b, 1c were determined. See from Fig. S1a (ESI), the peaks at 273 nm (ε = 85,860), 278 nm (ε = 79,540) and 275 nm (ε = 84,150) for 1a, 1b and 1c are allocated to π–π* transitions of intraligands. As shown in Fig. S1b (ESI), the compounds 1a, 1b, 1c emit a weak luminescence with a maximum emission peak at 563 (λ_{ex} = 400 nm), 562 (λ_{ex} = 400 nm) and 565 nm (λ_{ex} = 275 nm).

In PBS solution, UV–Vis spectra were applied to detect the stability of 1a, 1b, 1c, 1alip, 1blip, 1clip, 1aTlip, 1bTlip and 1cTlip at 0 and 24 h. As shown in Fig. S2 (ESI), we found no change in the peak shapes of 1a, 1b, 1c, 1alip, 1blip, 1clip, 1aTlip, 1bTlip and 1cTlip, indicating a stable existence of compounds and liposome-entrapped compounds at room temperature.

We determined the purity of 1a, 1b, 1c using high performance liquid chromatography (HPLC) with methanol and water as mobile phase, the volume ratios of methanol and water are 70:30 for 1a, 60:40 for 1b, 80:20 for 1c. As shown in Fig. S3 (ESI), during the 30 min period, we discovered only a main peak, the purity values for 1a, 1b, 1c calculated from the peak area are 98.41 %, 97.50 % and 96.54 %.

The peaks in the IR spectra at 3332, 3373, 3389 and 3329 cm^{-1} for ligand NNIP, 1a, 1b, 1c are allocated to N–H (imidazole ring) stretching vibration, while the C–H stretching vibration was observed at 3066 cm^{-1} for NNIP, 3040 cm^{-1} for 1a, 3041 cm^{-1} for 1b and 3043 cm^{-1} for 1c. The stretching vibration for P–F (PF_6^-) bond was found at 853 cm^{-1} for 1a, 844 cm^{-1} for 1b, 854 cm^{-1} for 1c, whereas its bending vibration

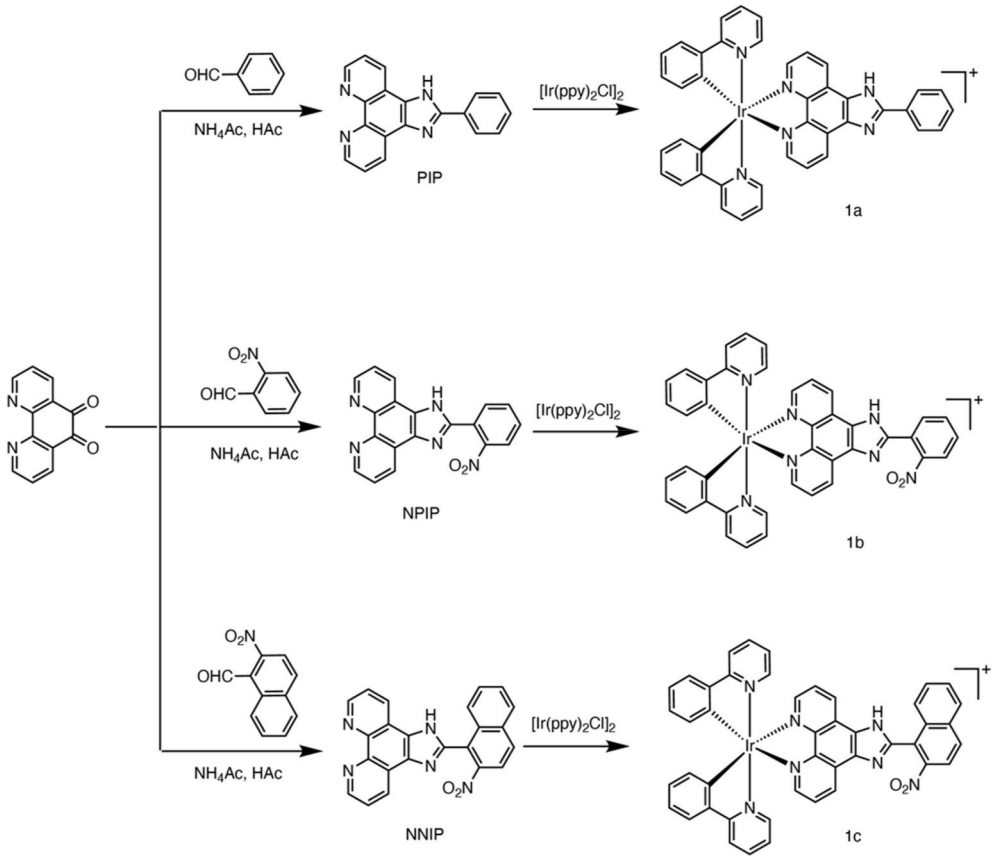

Scheme 1. Synthetic routes of ligands and compounds 1a, 1b, 1c.

locates at 557, 557 and 556 cm^{-1} for 1a, 1b and 1c, the stretching and bending vibration for P–F bond in NNIP were not observed, which indicates that the compounds were successfully synthesized.

In the HRMS assay, we found the molecular weights of 1a, 1b and 1c were consistent between the determined and calculated values. Owing to probably rapid exchange, the peak of the proton bonded to nitrogen in the imidazole ring was not discovered in the ^{1}H NMR spectra, similar results were observed in other iridium(III) compounds [7,9]. Additionally, we also found that the peaks at 172.59 ppm for 1b, 172.55 ppm for 1c are allocated for C atoms bonded with $–NO_2$ in the ^{13}C NMR spectra.

2.2. Preparation and characterization of liposomes

Liposomes are regarded as a potent drug delivery mechanism due to their variable structure, lack of immunogenicity, and lack of toxicity. Furthermore, the stability of the liposomes is strongly connected to their encapsulation rate, polydispersity index (PDI), and particle size potential. We used thin film dispersion method to prepare ordinary and targeted liposomes. Fig. S4a (ESI) shows that 1alip, 1blip, 1clip, 1aTlip, 1bTlip and 1cTlip show light-yellow. The encapsulation rates for 1a, 1b and 1c in the 1alip, 1blip, 1clip, 1aTlip, 1bTlip and 1cTlip are 90.31 %, 86.32 %, 84.25 %, 86.54 %, 89.49 % and 89.67 %, respectively. The mean particle sizes for 1alip, 1blip, 1clip, 1aTlip, 1bTlip and 1cTlip are 103.07 ± 1.9, 94.4 ± 0.7, 94.1 ± 0.7, 83.0 ± 1.2, 87.9 ± 2.6 and 93.3 ± 2.4 nm, respectively (Fig. S4b, ESI). The PDIs for 1alip, 1blip, 1clip, 1aTlip, 1bTlip and 1cTlip are 0.132 ± 0.012, 0.200 ± 0.006, 0.233 ± 0.003, 0.231 ± 0.006, 0.287 ± 0.013 and 0.264 ± 0.024. The PDI values are less than 0.3, indicating that the liposomes were homogeneous and stable. The zeta potentials were determined to be −83.74, −63.70, −58.56, −66.49, −64.26, and −60.77 mV for 1alip, 1blip, 1clip, 1aTlip, 1bTlip and 1cTlip (Fig. S4c, ESI). In summary, the particle size, low PDI values and zeta potentials show that the ordinary or targeted liposomes are very high stability [34,35].

2.3. pK_a and pH measurement

Compounds 1a, 1b, 1c were dissolved in $CH_3CN–H_2O$, using pH meter to measure the pH values. The pH values of 6.90, 6.64 and 6.81 for 1a, 1b and 1c indicate that the compounds show weak acidity. According to pH partition theory [36,37], once inside cells, the compounds with weak acid will enter alkaline compartments mitochondria [38]. Hence, the compounds can enter the mitochondria. Additionally, pk_a values play an important role in drug properties including distribution, adsorption, metabolism and so on [39]. Manallack reported that the compounds may enter cancer cells in the range of $4 < pK_a < 10$ [40]. Fig. S5 (ESI) reveals that the pK_a values of 1a, 1b and 1c are 6.85, 6.62 and 6.65, respectively. The pK_a values fall well within the scope of $4 < pK_a < 10$, indicating that the compounds may enter the cells.

Note: In the following cell experiments, the excited and emission wavelengths of dyes are listed as following: DAPI (2-(4-Amidinophenyl)-6-indolecarbamidine dihydrochloride): λ_{ex} = 340 nm, λ_{em} = 488 nm, DCFH-DA (2′,7′-Dichlorodihydrofluorescein diacetate): λ_{ex} = 488 nm, λ_{em} = 525 nm, Mito-Tracker Red: λ_{ex} = 579 nm, λ_{em} = 599 nm, Fluo-3 AM (Fluo-3-pentaacetoxymethyl ester): λ_{ex} = 506 nm, λ_{em} = 526 nm, JC-1 monomers: λ_{ex} = 514 nm, λ_{em} = 529 nm, JC-1 aggregates: λ_{ex} = 585 nm, λ_{em} = 590 nm, BODIPY 581/591C11 oxidized: λ_{ex} = 500 nm, λ_{em} = 510 nm, BODIPY 581/591C11 reduced: λ_{ex} = 581 nm, λ_{em} = 591 nm, Annexin V-FITC: λ_{ex} = 488 nm, λ_{em} = 525 nm, propidium iodide (PI): λ_{ex} = 535 nm, λ_{em} = 615 nm.

In all the following cell experiments, IC_{50} concentrations for 1a, 1b, 1c, 1alip, 1blip, 1clip, 1aTlip, 1bTlip, 1cTlip are 1a (8.0 μM), 1b (8.6 μM), 1c (17.0 μM), 1alip (8.0 μM), 1blip (8.6 μM), 1clip (17.0 μM), 1aTlip (6.0 μM), 1bTlip (7.3 μM) and 1cTlip (9.7 μM).

2.4. Cellular uptake studies

Cell uptake of iridium(III) compounds by HepG2 cells was studied under a fluorescent microscope to observe whether iridium(III) compounds can enter the cells. See from Fig. 1, after a 6 h treatment of HepG2 cells with the compounds and their liposomes, the cell nuclei were stained blue with 4′,6-diamidino-2-phenylindole (DAPI), while 1a, 1b and 1c emit weak green fluorescence, a bright green fluorescence was seen in 1alip, 1blip, 1clip, 1aTlip, 1bTlip and 1cTlip-treated groups. The merge demonstrated that the liposomes 1alip, 1blip, 1clip, 1aTlip, 1bTlip and 1cTlip access the cells and focus on the cell nuclei. Fig. S6 (ESI) indicates that 1alip, 2alip and 3alip cause an increase of green fluorescence intensity by 5.30, 3.99 and 1.95 times, the targeted liposomes 1aTlip, 1bTlip and 1cTlip induce an increase by 7.52, 4.11 and 3.45 times, while 1a, 1b and 1c increased by 5.13, 1.34 and 1.18 times than the original. Consequently, low cell uptaken amounts of 1b and 1c agree with their cytotoxic activity.

2.5. Anti-proliferative ability in vitro

The antiproliferative ability of compounds 1a, 1b, 1c toward HepG2, BEL-7402, SK-Hep1, LO2 was assessed using MTT. After 1.56, 3.125, 6.25, 12.5, 25, 50, 100 μM of 1a, 1b or 1c were added to the above cells for 48 h, the IC_{50} values were obtained (Table 1). We observed that 1a demonstrates moderately antiproliferative active against BEL-7402, HepG2, Sk-Hep1 and non-cancer LO2 cells, whilst 1b and 1c showed non-toxic with IC_{50} values more than 100 μM. To explore why 1a showed moderate cytotoxic activity, while 1b and 1c displayed no cytotoxicity, we determined the partition coefficient (log*P*), log*P* values for 1a, 1b, 1c are 0.276 ± 0.035, −0.438 ± 0.026, −0.700 ± 0.042. The low log*P* values suggest that compounds 1b and 1c have poor lipophilicity, which results in a less amount of the compounds to enter the cells. In addition, the cell uptake also confirms the less amounts of 1b and 1c to enter the cells. Therefore, 1b and 1c show low antiproliferative ability to inhibit the cell growth. To improve the anti-cancer efficiency, compounds 1a, 1b, 1c were loaded in the ordinary and targeted liposomes to produce 1alip, 1blip, 1clip and targeted 1aTlip, 1bTlip and 1cTlip. Surprisingly, 1alip, 1blip and 1clip exhibit high or moderate anti-cancer effect on BEL-7402, HepG2, SK-Hep1 cells, while the targeted liposomes 1aTlip, 1bTlip, 1cTlip show higher antiproliferative activity than ordinary liposomes 1alip, 2alip, 3alip. Particularly, 1aTlip, 1bTlip, 1cTlip reveal the highest antiproliferative activity toward HepG2 cells with a low IC_{50} value of 5.9 ± 0.2, 7.3 ± 0.1 and 9.7 ± 0.7 μM. Hence, the targeted liposomes greatly enhance the antiproliferative ability. 1alip, 1blip, 1clip, 1aTlip, 1bTlip and 1cTlip display moderate anti-cancer efficacy on non-cancer LO2 cells. Additionally, we also discovered that 1alip, 1blip, 1aTlip and 1bTlip exhibit higher anticancer efficiency than cisplatin and $[Ir(bzq)_2(DIPH)]PF_6$-loaded liposomes (IC_{50} = 16.0 ± 1.4 μM) [41] on HepG2 cells. Owing to 1aTlip, 1bTlip, 1cTlip showing the highest antiproliferative ability against HepG2, therefore, in the following cell experiments, we investigate anti-cancer effect of the compounds and compounds-loaded liposomes on HepG2 cells.

2.6. Wound healing, colony formation, cell cycle arrest

Cancer is characterized by infinite cell growth and metastasis [42]. To further assess the ability of compounds hindering cell growth and migration, we performed cell cloning and scratch tests. As depicted in Fig. S7a (ESI), the ordinary liposomes 1alip, 1blip, 1clip and targeted liposomes 1aTlip, 1bTlip, 1cTlip can validly prevent the cell migration, while 1a, 1b or 1c show a low ability to hinder the cell migration. On the other hand, in a variety of human cancers, such as hepatocellular carcinoma, colon cancer, and breast cancer, overexpressed FAK protein was observed. It can mediate a variety of cell function-related signaling, including cell proliferation, migration, and adhesion [43,44].

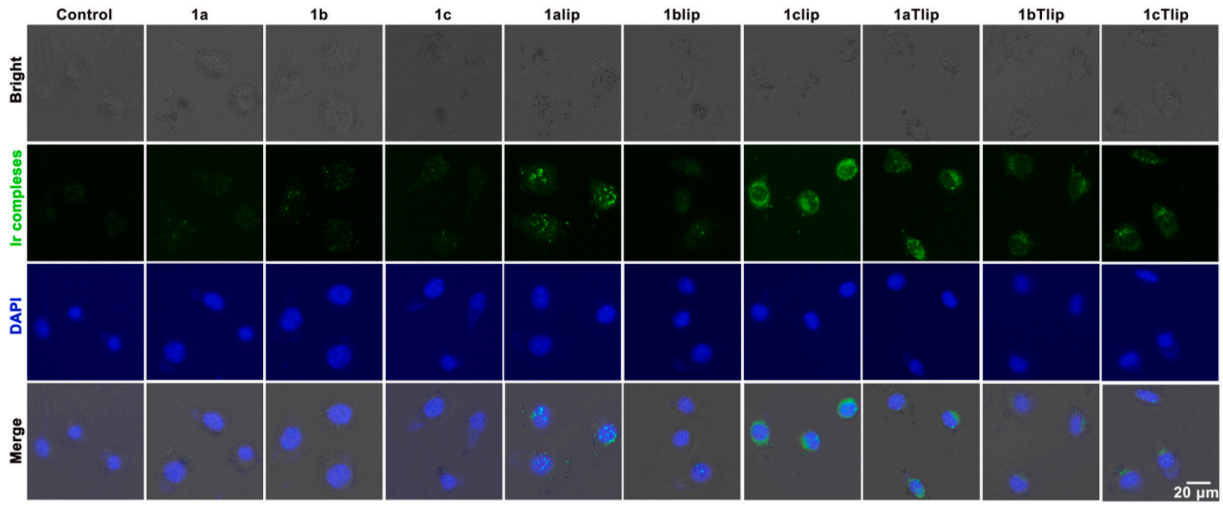

Fig. 1. Cellular uptake was measured while HepG2 cells were exposed to the compounds and compound-loaded liposomes 1a (8.0 μM), 1b (8.6 μM), 1c (17.0 μM), 1alip (8.0 μM), 1blip (8.6 μM), 1clip (17.0 μM), 1aTlip (6.0 μM), 1bTlip (7.3 μM) and 1cTlip (9.7 μM) for 6 h and stained with DAPI (λ_{ex} = 340 nm).

Table 1
IC_{50} values (μM) of complexes and liposomes toward cancer cells for 48 h.

Compounds	BEL-7402	HepG2	SK-Hep1	LO2
1a	13.78 ± 0.55	20.9 ± 1.2	22.4 ± 1.2	32.1 ± 0.8
1b	>100	78.2 ± 3.7	>100	>100
1c	>100	>100	>100	>100
1alip	8.9 ± 0.4	7.9 ± 0.1	12.9 ± 0.8	10.8 ± 0.3
1blip	12.9 ± 0.5	8.6 ± 0.2	27.8 ± 0.9	16.7 ± 0.5
1clip	16.4 ± 0.4	16.9 ± 0.5	22.5 ± 1.5	14.7 ± 0.4
1aTlip	8.6 ± 0.2	5.9 ± 0.2	9.1 ± 0.1	10.8 ± 0.1
1bTlip	11.1 ± 0.2	7.3 ± 0.1	8.1 ± 0.6	9.8 ± 0.3
1cTlip	10.4 ± 0.3	9.7 ± 0.7	20.3 ± 0.8	11.3 ± 0.6
cisplatin	14.8 ± 3.4	9.4 ± 1.5	nd	18.2 ± 2.6

nd: not determination.

To further assess the ability of the compounds and compound-loaded liposomes to prevent HepG2 cell colony, through a continuous seven day-treatment of HepG2 with 1a (8.0 μM), 1b (8.6 μM), 1c (17.0 μM), 1alip (8.0 μM), 1blip (8.6 μM), 1clip (17.0 μM), 1aTlip (6.0 μM), 1bTlip (7.3 μM) and 1cTlip (9.7 μM), cells were washed four times and stained. As shown in Fig. S7b (ESI), we observed that the live cells (purple) decreased in the 1alip-1clip and 1aTlip-1cTlip-treated groups. Therefore, ordinary 1alip, 1blip, 1clip and targeted liposomes 1aTlip, 1bTlip and 1cTlip can validly inhibit the cell colony, while compounds 1a, 1b and 1c demonstrate a weak efficacy on inhibiting the cell colony in HepG2 cells.

By regulating cell cycle, inhibition of cancer cell proliferation is an important strategy for cancer treatment. To assess the efficacy of the compounds and compound-encapsulated liposomes on the progression, we measured cell cycle distribution. See from Fig. 2a, at G0/G1 phase, a 24 h exposure of HepG2 to 1alip, 1blip, 1clip, 1aTlip, 1bTlip and 1cTlip (IC_{50} concentration) led to an increase of 19.70, 9.61, 12.12, 21.67, 16.64 and 21.47 %, meanwhile, a reduction at S period was also discovered. Compounds 1a, 1b and 1c exhibit a poor antiproliferative ability, targeted liposomes 1aTlip, 1bTlip and 1cTlip show the highest ability to prevent the cell proliferation among the compounds and compounds-loaded liposomes. The results show that 1alip, 1blip, 1clip, 1aTlip, 1bTlip and 1cTlip exert anti-cancer activity through hindering cell growth in G0/G1 period.

On the other hand, cycle protein CDK2 (cyclin-dependent kinase 2) plays a key role in the progression of cell cycle [45]. Inhibition of CDK2 activity can validly hinder HepG2 cell proliferation [46]. As shown in Fig. 2b, we observed that ordinary liposomes 1alip, 1blip, 1clip, and targeted liposomes downregulated the expression of CDK2, which further confirms at the G0/G1 period, 1alip, 1blip, 1clip, 1aTlip, 1bTlip and 1cTlip hinder cell growth. Additionally, Fig. 2b demonstrated that ordinary liposomes 1alip, 1blip, 1clip, and targeted liposomes 1aTlip, 1bTlip and 1cTlip can validly inhibit FAK protein expression, which suggests that 1alip, 1blip, 1clip, 1aTlip, 1bTlip and 1cTlip may validly hinder HepG2 cell migration via inhibiting the FAK signaling pathway.

2.7. Exploration of apoptotic mechanism with RNA-sequence assay

To explore the apoptotic mechanism, RNA-sequence assay was carried out. Using 2 × IC_{50} concentration 1alip and 1aTlip to treat HepG2 cells, after 24 h, the RNA was extracted, and the RNA-sequencing was analyzed to obtain heatmap (Fig. 3a for 1alip, 3b for 1aTlip), upset and venn map (c and d), GO enrichment and KEGG enrichment maps. Observing from Fig. 3c and d, in 1alip group, 1462 genes showed significant changes in the expression, in which the expression of 667 and 795 genes was increased and reduced. In 1aTlip-treated group, 1026 genes were dysregulated, including 472 upregulated and 554 downregulated genes. Notably, we found that the same expression of 817 genes in 1alip and 1aTlip groups was observed. The above clustering analysis of the dysregulated genes showed that the gene expression profiles in the control, 1alip and 1aTlip groups were significantly distinguishable.

The results of GO Enrichment analysis for 1alip and 1aTlip are shown in Fig. 3e and g, differentially expressed genes are heavily enriched mainly in cellular biological processes (BP) involved in tissue development, response to stimuli, response to stimulus, response to organic substance, development of multicellular organism and cellular response to chemical stimulus.

KEGG enrichment analysis showed that 1alip and 1aTlip (Fig. 3f and h) induce cell death via the same signaling pathways, including p53 signaling pathway, apoptosis, autophagy, MAPK signaling pathway, glutamate glycine metabolism and cell adhesion molecules. In addition, 1aTlip induces cell death through PI3K/AKT signaling pathway.

2.8. Annexin V and PI staining apoptosis and mechanism studies

Drugs access cell to damage DNA and prevent the replication of DNA, leading to apoptosis [47]. Most cytotoxic anti-cancer drugs have been reported to cause cell apoptosis [48]. Main aim of cancer chemotherapy is to cause apoptosis in tumor cells after exposure to anti-cancer drugs. Apoptotic cells have morphological features such as chromatin condensation, DNA breakage, apoptotic vesicle formation and cell

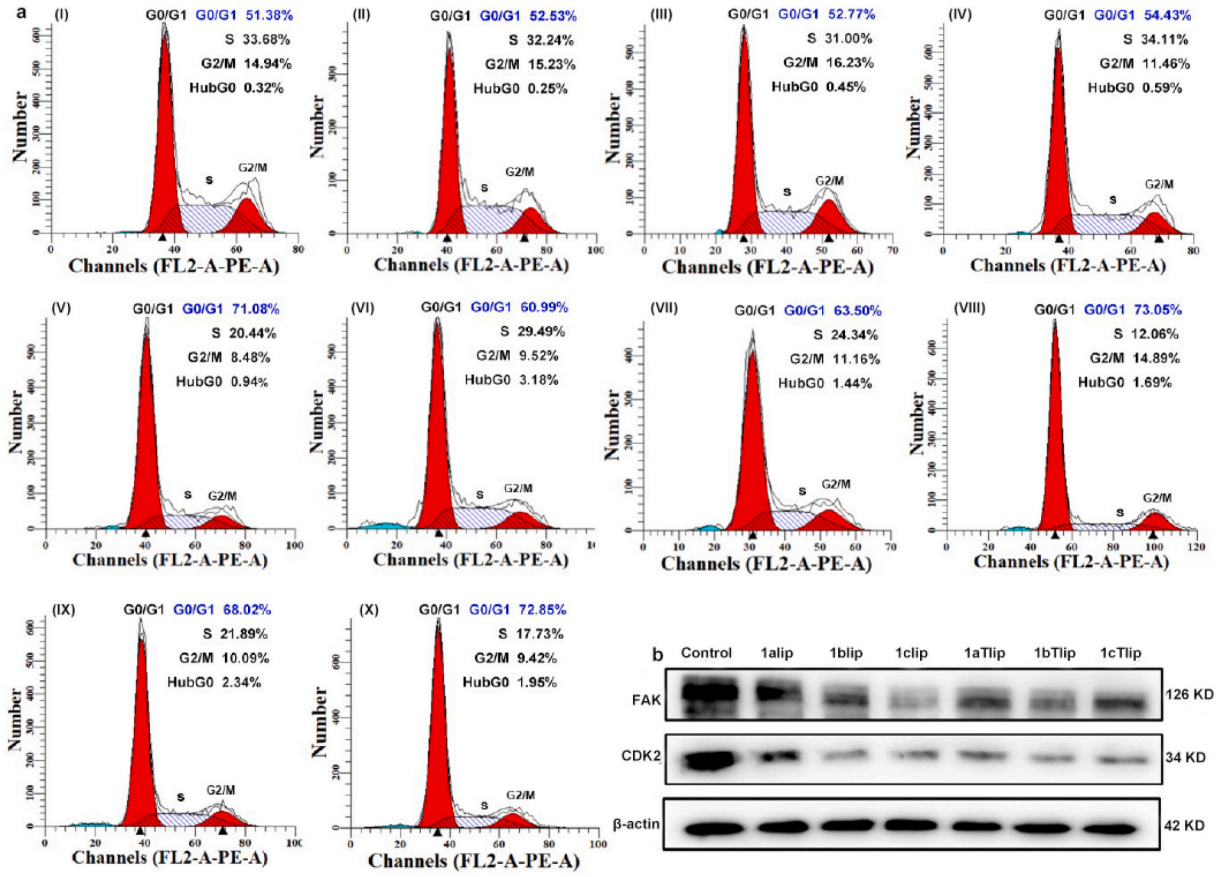

Fig. 2. (a) Cell cycle distribution of HepG2 (I) exposed to 1a (8.0 μM II), 1b (8.6 μM III), 1c (17.0 μM IV), 1alip (8.0 μM V), 1blip (8.6 μM VI), 1clip (17.0 μM VII), 1aTlip (6.0 μM VIII), 1bTlip (7.3 μM IX), 1cTlip (9.7 μM X), (b) expression of FAK and CDK2 after HepG2 cells were exposure to 1a (8.0 μM), 1b (8.6 μM), 1c (17.0 μM), 1alip (8.0 μM), 1blip (8.6 μM), 1clip (17.0 μM), 1aTlip (6.0 μM), 1bTlip (7.3 μM) and 1cTlip (9.7 μM) for 24 h.

shrinkage, which are associated with endogenous nucleic acid endonuclease activity. Wang et al. found that three newly synthesized iridium (III) compounds exert anti-cancer activity via mitochondria-endoplasmic reticulum pathway [49]. It was found that phosphatidylserine was recognized by Annexin V but not stained by propidium iodide (PI) [50]. The IC_{50} dose of compounds and compounds-loaded liposomes were used to treat HepG2 cells, we determined the percentage of live cell, early, late apoptosis. As can be seen in Fig. 4a, in 1a, 1b, 1c-treated groups, the proportion of early apoptotic cells is 6.37 %, 5.25 % and 5.38 %, respectively. We discovered that compounds 1a, 1b, 1c reveal low apoptotic efficiency. However, ordinary liposomes 1alip, 1blip, 1clip and targeted liposomes 1aTlip, 1bTlip and 1cTlip induce an increase of 12.87, 16.47, 6.97, 15.67, 17.37 and 13.67 % comparison to the control. The targeted liposomes-entrapped compounds 1aTlip, 1bTlip and 1cTlip show higher apoptotic effect than 1alip, 1blip and 1clip. The data obtained suggest that the targeted liposome-encapsulated compounds show the highest apoptotic efficacy among these compounds and their liposomes.

To further investigate the mechanism of 1alip, 1blip, 1clip and targeted liposomes 1aTlip, 1bTlip and 1cTlip inducing apoptosis in HepG2 cells, expression of Bcl-2 family proteins was explored. As depicted in Fig. 4b and 24 h exposure of HepG2 to 1alip, 1blip, 1clip, 1aTlip, 1bTlip and 1cTlip (IC_{50} concentration) led to an increase of Bax, caspase 3, and a decrease of Bcl-2 expression, we also observed that PARP (poly(ADP-ribose) polymerase) was cleaved. On the other hand, Bax/Bcl-2 ratio is proportional to the apoptosis [51]. As expected, it is clear from Fig. 4b that increase in the expression of Bax and decrease of Bcl-2 resulted in an increase of Bax/Bcl-2 ratio, which further confirms that 1alip, 1blip, 1clip, 1aTlip, 1bTlip and 1cTlip induce apoptosis through revitalizing caspase 3, cleaving PARP and controlling the expression of Bcl-2 family proteins.

Furthermore, inhibition of PI3K/AKT/m-TOR can enhance the activation of autophagic signaling and induces tumor cell death [52–55]. AKT as an essential mediator plays a key role in the PI3K signaling pathway [56], inhibition of AKT expression will promote apoptosis. As shown in Fig. 4b, 1alip and 1blip, 1clip, 1aTlip, 1bTlip and 1cTlip downregulated the expression of PI3K, mTOR and AKT. Additionally, we examined the expression of phosphorylation level of p-mTOR, p-PI3K, see from Fig. 4c, 1alip and 1blip, 1clip, 1aTlip, 1bTlip and 1cTlip also reduce the expression of p-mTOR and p-PI3K. These results suggest that the ordinary liposomes or targeted liposomes promote apoptosis by controlling the expression of Bcl-2 family proteins, hindering the signal pathway of PI3K/AKT/mTOR.

2.9. *Co-location and mitochondrial dysfunction*

Mitochondria serve as the command-and-control center of apoptosis, and induction of apoptosis decreases the mitochondrial membrane potential [57]. As can be seen in Fig. 5a, the mitochondria were stained red with Mito Tracker Deep Red, we found that compounds 1a, 1b, 1c, liposomes 1alip, 1blip, 1clip, targeted liposomes 1aTlip, 1bTlip and 1cTlip colocalized strongly in the mitochondria. The results are consistent with those obtained from the pH determination. To evaluate the correlation, we calculated Pearson's colocalization coefficients (PCC) to be 0.9977 for 1a, 0.9981 for 1b, 0.9977 for 1c, 0.9976 for 1alip, 0.9947 for 1blip, 0.9988 for 1clip, 0.9960 for 1aTlip, 0.9940 for 1bTlip, and 0.9954 for 1cTlip, respectively, which hints a positive correlation. The obtained results demonstrate that 1a, 1b, 1c, 1alip, 1blip, 1clip, 1aTlip,

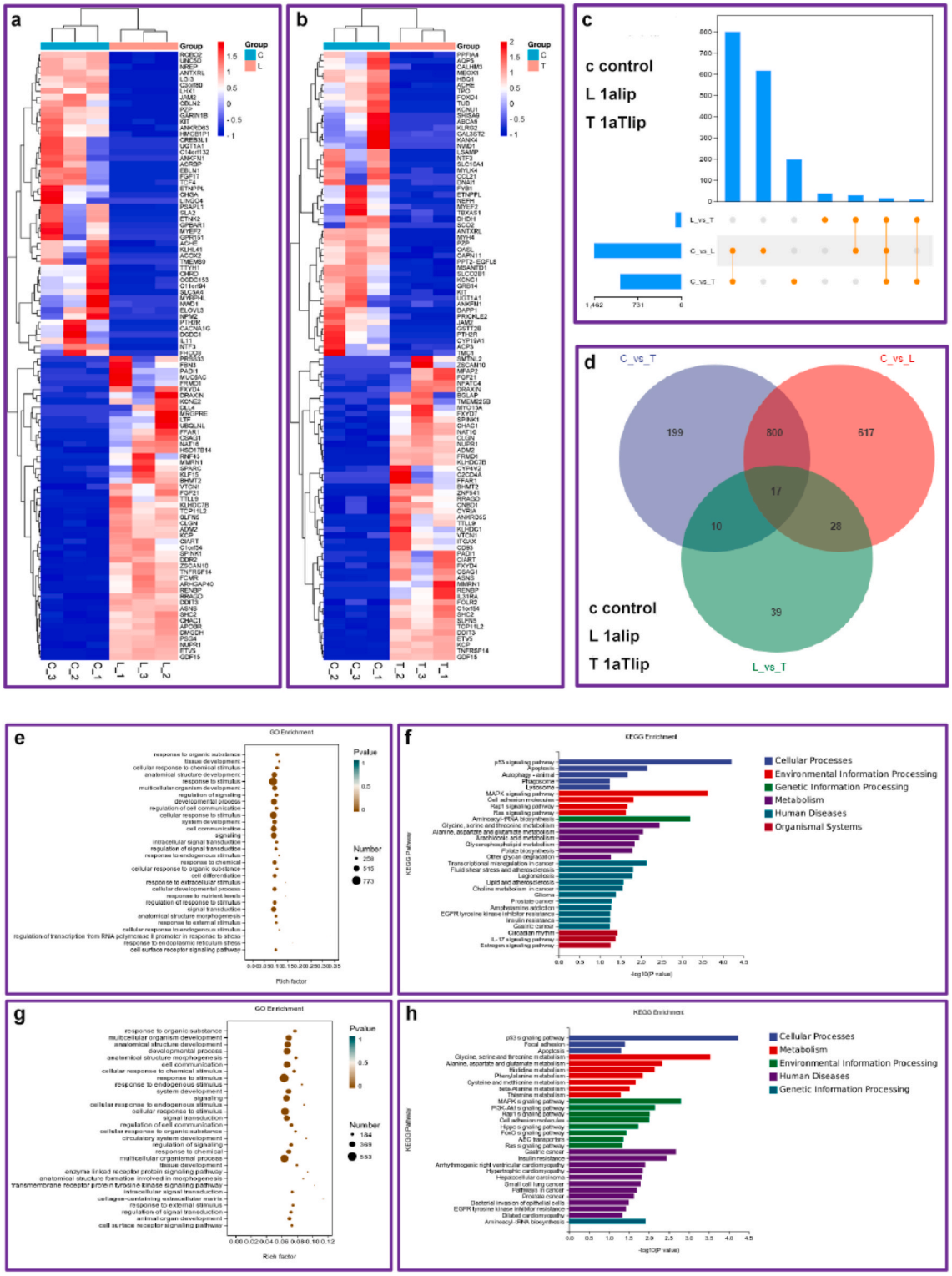

Fig. 3. Analysis of single-cell RNA sequencing heatmap for 1alip (a) and 1aTlip (b), (c and d) upset and venn map for 1alip and 1aTlip. (e and f) GO and KEGG enrichment for 1alip, (g and h) GO and KEGG for 1aTlip while HepG2 cells were treated with 2 × IC_{50} concentration 1alip and 1aTlip for 24 h.

1bTlip and 1cTlip interact on the mitochondria.

To investigate whether iridium(III) compounds and their liposomes trigger apoptotic through mitochondrial signaling pathway, the efficacy of metal compounds and liposome entrapped compounds on the variation of mitochondrial membrane potential (Δ_{MMP}) was examined using an indicator of JC-1 (5,5′,6,6′-tetrachloro-1,1′,3,3′-tetraethylbenzimidazolyl carbocyanine iodide). Aggregates of JC-1 produces bright red fluorescence matching with high MMP, while in the mitochondrial damage state, aggregates JC-1 are converted into monomer JC-1 (green fluorescence matching with a low MMP) [9]. Observe from Fig. 5b, the change of red (control) into the green fluorescence (treated groups) indicates that compounds, ordinary liposomes, and targeted liposomes encapsulated compounds cause a decrease in the MMP. Additionally, ratio of red/green fluorescence was quantitatively determined. To

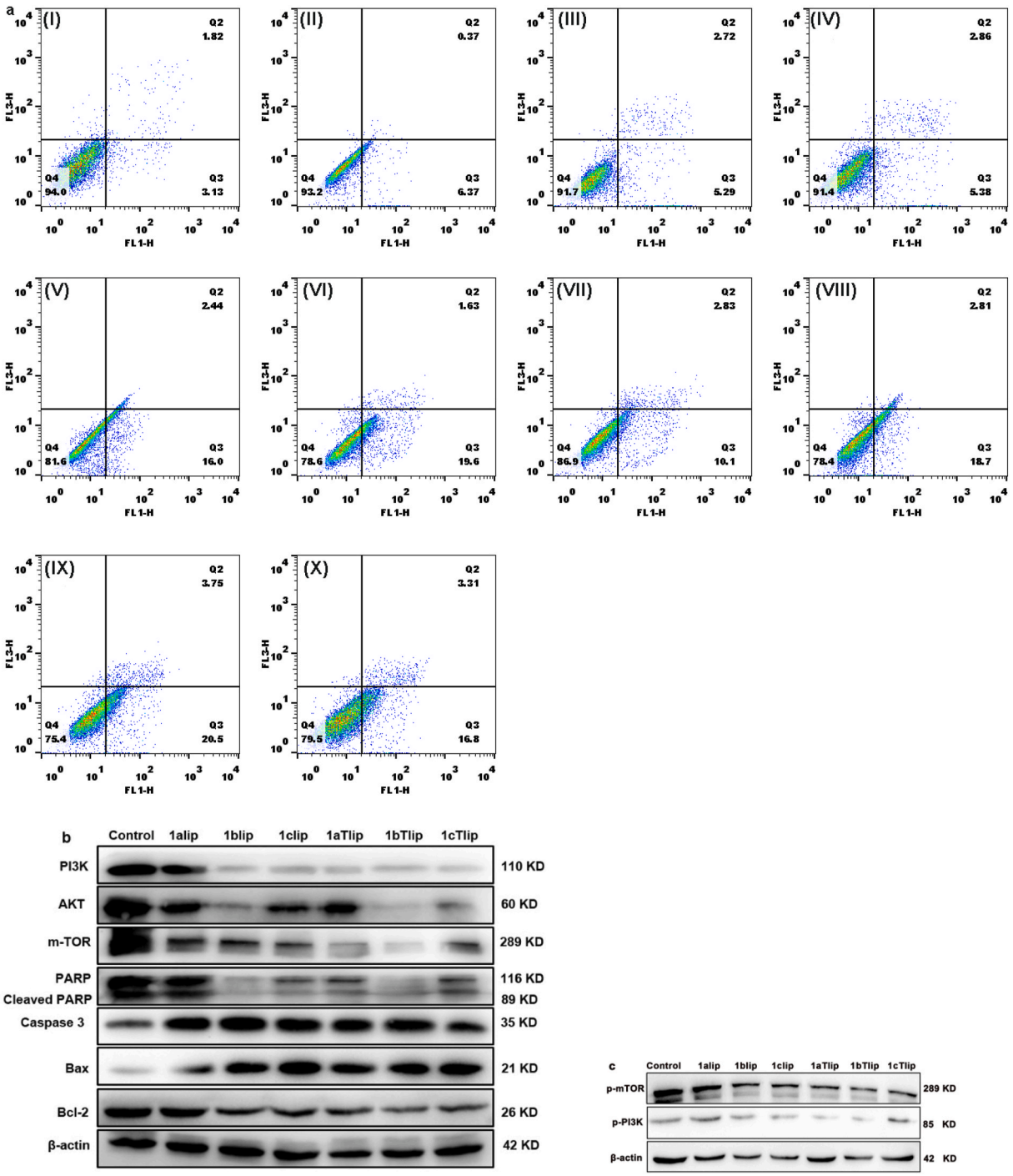

Fig. 4. (a) Apoptosis assays of HepG2 cells (I) incubated with 1a (II), 1b (III), 1c (IV), 1alip (V), 1blip (VI), 1clip (VII), 1aTlip (VIII), 1bTlip (IX), 1cTlip (X) at IC_{50} concentration for 24 h. (b) assay of expression of proteins after HepG2 cells were treated with IC_{50} concentration 1alip, 1blip, 1clip, 1aTlip, 1bTlip and 1cTlip for 24 h, (c) The expression of p-mTOR and p-PI3K while HepG2 cells were treated with IC_{50} concentration 1alip, 1blip, 1clip, 1aTlip, 1bTlip and 1cTlip for 24 h.

eliminate the disruptions of the green fluorescence caused by the compounds or compound-loaded liposomes, 1a, 1b, 1c, 1alip, 1blip, 1clip, 1aTlip, 1bTlip and 1cTlip were used as references. As depicted in Fig. S8 (ESI), 1a, 1b, 1c, 1alip, 1blip, 1clip, 1aTlip, 1bTlip and 1cTlip caused a decline in the red/green ratio comparison with the control, moreover, compounds 1a, 1b, 1c exhibit a poor effect on the change in MMP. The gained results hint that the liposome-loaded metal compounds act on the mitochondria, then cause a reduction of MMP, lastly, lead to mitochondrial dysfunction to trigger apoptosis.

2.10. Determination of intracellular Ca^{2+} levels

In disease and stress states, the cellular environment is disrupted, leading to an increase in free calcium ions [58]. Calcium ion concentrations are closely related to apoptosis, cellular autophagy, and cell proliferation. To explore the impact of compounds and compound-loaded liposomes on the change of Ca^{2+} concentration using Fluo-3 AM as a probe. In the presence of esterase, Fluo-3 AM is cleaved into Fluo-3, binding of Fluo-3 with Ca^{2+} will produce a bright fluorescence. As shown in Fig. S9 (ESI), we found that only an increase by 1.05,

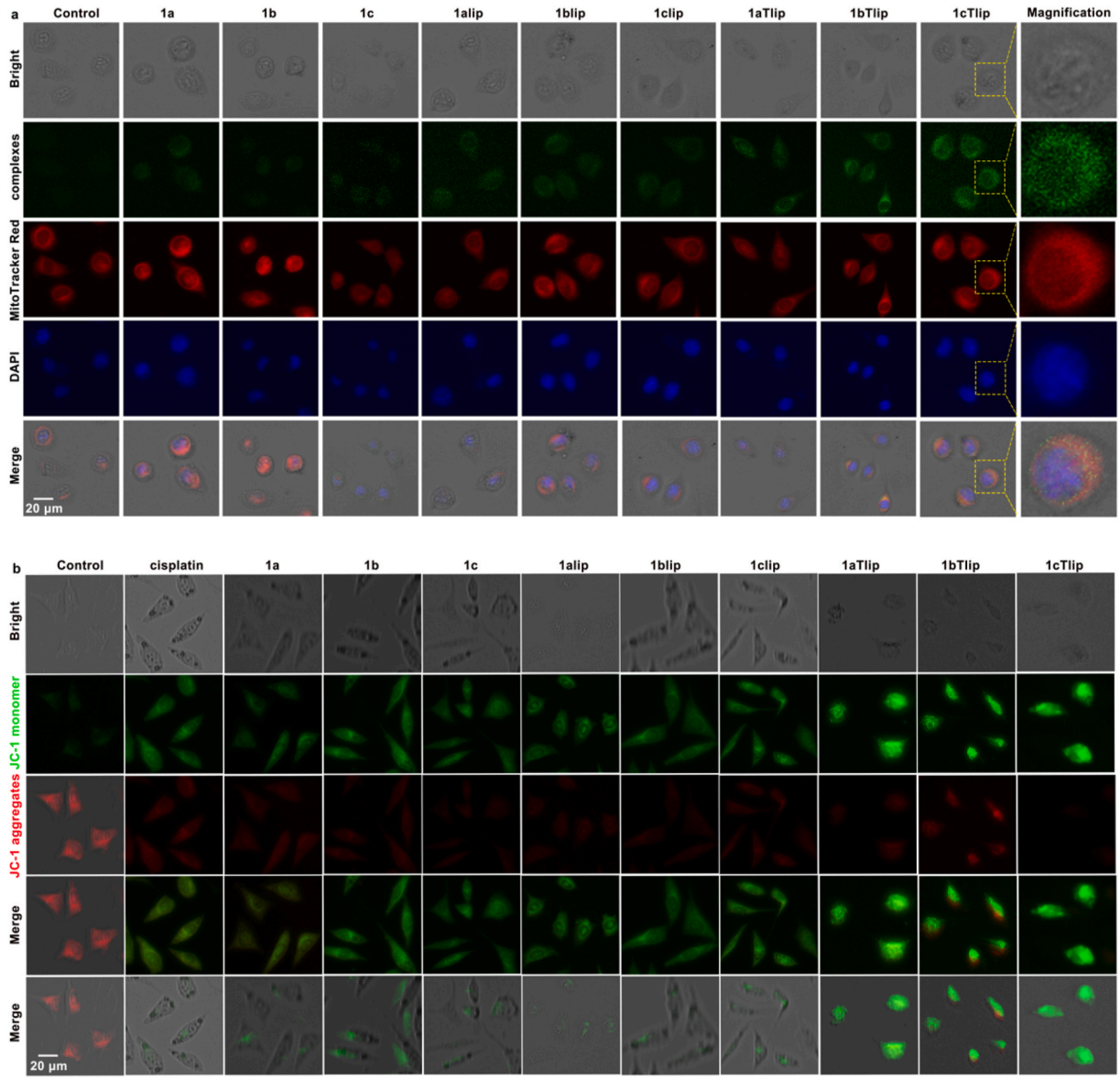

Fig. 5. (a) The location of the compounds and compounds entrapped liposomes in the Mitochondria after HepG2 cells were exposed to 1a, 1b, 1c, 1alip, 1blip, 1clip, 1aTlip, 1bTlip and 1cTlip for 4 h. (b) The changes of mitochondrial membrane potential while HepG2 cells were exposed to cisplatin (positive control), 1a, 1b, 1c, 1alip, 1blip, 1clip, 1aTlip, 1bTlip and 1cTlip for 24 h. The concentrations of 1a, 1b, 1c, 1alip, 1blip, 1clip, 1aTlip, 1bTlip and 1cTlip are 8.0, 8.6, 17.0, 8.0, 8.6, 17.0, 6.0, 7.3 and 9.7 μM.

1.16 and 1.36 times in 1a-1c-treated group comparison with control. However, the calcium ion concentrations in the 1alip, 1blip, 1clip and the targeted liposomes, 1aTlip, 1bTlip and 1cTlip-treated groups were significantly increased by 8.61, 3.06,1.84 times, and 8.82, 8.51 and 3.10 times than original. Compounds 1a, 1b, 1c show a weak ability to raise Ca^{2+} concentration, while the targeted liposomes 1aTlip-1cTlip reveal the highest ability to enhance the intracellular Ca^{2+} concentration. The results demonstrate that ordinary and the targeted liposomes entrapped compounds can elevate the intracellular Ca^{2+} concentration.

2.11. Reactive oxygen species assay

ROS inducing lipid peroxidation plays a key role in apoptosis, autophagy, and ferroptosis [59]. To eliminate the disruption, in the assay of ROS, the compounds and liposome-encapsulated compounds were used as references. As shown in Fig. S10 (ESI), compound 1a, 1b and 1c display a low effect on the ROS content. However, 24 h treatment of HepG2 cells with 1alip, 1blip, 1clip and targeted liposomes 1aTlip, 1bTlip and 1cTlip caused an increase of DCF fluorescence by 83.2, 17.5, 7.58, 80.74, 11.7 and 37.8 times than that in the control. The targeted liposome 1cTlip show higher efficiency on ROS than ordinary liposomes 1clip. Unexpectedly, liposomes 1blip and 1clip exhibit higher efficacy on ROS than their targeted liposomes 1aTlip and 1bTlip. Therefore, 1alip-1clip and 1aTlip-1cTlip can enhance ROS content. Taken together, we consider that liposomes 1alip-1clip and targeted liposomes 1aTlip-1cTlip cause an increase in ROS content.

2.12. Autophagy studies

Autophagy is closely associated with a variety of human diseases and physiology, including hepatocellular carcinoma. Excessive autophagy may lead to autophagic cell death. LC3 is a marker of autophagy, and during autophagy formation, the cytoplasmic type LC3-I is converted to the (autophagosome) membrane type LC3-II. Beclin-1 is an essential molecule in autophagosome formation, which mediates the localization of other autophagic proteins to autophagic vesicles, thus regulating the

formation and maturation of mammalian autophagosomes [60,61]. As can be seen from Fig. S11 (ESI), comparing with the control group, LC3-I in the liposomes and targeted liposomes-treated group was transferred into LC3-II. Additionally, we also discovered an upregulation in the Beclin-1 expression. The results show that the liposomes and targeted liposomes can validly induce autophagy in HepG2 cells.

2.13. Ferroptosis exploration

(I) Assay of number of live cells

Enhancement of intracellular ROS is closely related to ferroptosis. Ferrotin-1 (Fer-1) can inhibit incidence of ferroptosis [62]. To confirm whether the compounds and their liposomes can cause ferroptosis, using ordinary or targeted liposomes-loaded compounds as references, number of live cells was examined with or without Fer-1. See form Fig. 6a, the number of live cells (with Fer-1) increased comparison to 1alip, 1blip, 1clip, 1aTlip, 1bTlip and 1cTlip alone (without Fer-1). The number of live cells increased by 9.08, 7.11, 4.04, 11.90, 8.88 and 7.39 times for 1alip + Fer-1, 1blip + Fer-1, 1clip + Fer-1, 1aTlip + Fer-1, 1bTlip + Fer-1 and 1cTlip + Fer-1, respectively. The results indicate that 1alip, 1blip, 1clip, 1aTlip, 1bTlip and 1cTlip can cause ferroptosis.

(II) Detection of GSH and MDA levels

A decrease in glutathione (GSH) content in cells can increase the susceptibility of cancer cells to various forms of programmed death and to chemotherapy [63]. During apoptosis, GSH is oxidized to convert into glutathione disulfide (GSSG), reflecting a decrease in the ratio of GSH versus GSSG, hence, the change in GSH/GSSG redox status can be used as an indicator of the extent to which apoptosis occurs [64,65]. Malondialdehyde (MDA) is a hallmark by-product of the lipid peroxidation process. Levels of MDA, a product of lipid peroxidation, increase dramatically when the cells undergo oxidative stress. To further investigate the mechanism of the liposomes or targeted entrapped compounds promoting apoptosis, the intracellular levels of GSH and MDA were examined. As depicted in Fig. 6b, in the liposomes and targeted liposomes entrapped compounds groups, the GSH content decreased comparison to the control, especially, 1cTlip shows the highest effect on the reduction of GSH among the ordinary and targeted liposomes entrapped compounds. In addition, the ratio of GSH/GSSG decreased (Fig. 6c), it was caused by the reaction of GSH with ROS to generate GSSG, leading to reduction of GSH content. Additionally, it can be seen from Fig. 6d that the intracellular MDA levels enhanced in 1alip, 1blip, 1clip, 1aTlip, 1bTlip and 1cTlip-treated groups. The above results implied that 1alip, 1blip, 1clip, 1aTlip, 1bTlip and 1cTlip can lessen GSH amount and raise MDA amount and further induce lipid peroxidation.

(III) Lipid peroxidation detection

In the ferroptosis, lipid peroxidation was examined using 4,4-difluoro-5-(4-phenyl-1,3butadenyl)-4-bora-3a, 4a-diaza-sindacene-3-undecanoic acid (C11-BODIPY) as stained reagent. It is well known that red and green fluorescence represent low and high degree of lipid peroxidation, respectively [66,67]. As seen in Fig. 6e and f, in the control, we observed red fluorescence corresponding to low degree of lipid peroxidation, while we discovered bright green fluorescence matching with a high degree of lipid peroxidation in 1alip-1clip and targeted 1aTlip-1cTlip-treated groups. The results confirm that 1alip-1clip, 1aTlip-1cTlip can induce a lipid peroxidation.

(IV) Ferroptosis-related proteins expression

Ferroptosis can directly or indirectly prevent the expression of glutathione peroxidase 4 (GPX4), resulting in a decrease of intracellular antioxidant systems. While ROS generation in mitochondria causes cellular malfunction [68]. Ferroptosis is also characterized by the accumulation of lipid peroxidation, which can be initiated by the inhibition of biomarker of iron toxicity GPX4, disrupting the GSH/GSSG system and thus killing cells [69]. To determine whether GPX4 is involved in this process, we examined the expression of GPX4. As shown in Fig. 6g, the expression of GPX4 was significantly downregulated.

Autophagy can degrade ferritin, which promotes ferroptosis [70]. Therefore, we examined the expression of ferritin, as depicted in Fig. 6g, 1alip and 1blip, 1clip, 1aTlip, 1bTlip, 1cTlip downregulated the expression of ferritin, indicating that 1alip, 1blip, 1clip, 1aTlip, 1bTlip, 1cTlip can cause ferroptosis through autophagy to degrade the ferritin. Activation of HMGB1 (high mobility group protein 1) has been shown to increase ROS content, which triggers ferroptosis [71]. Fig. 6g showed that 1alip, 1blip, 1clip, 1aTlip, 1bTlip, 1cTlip led to a significant

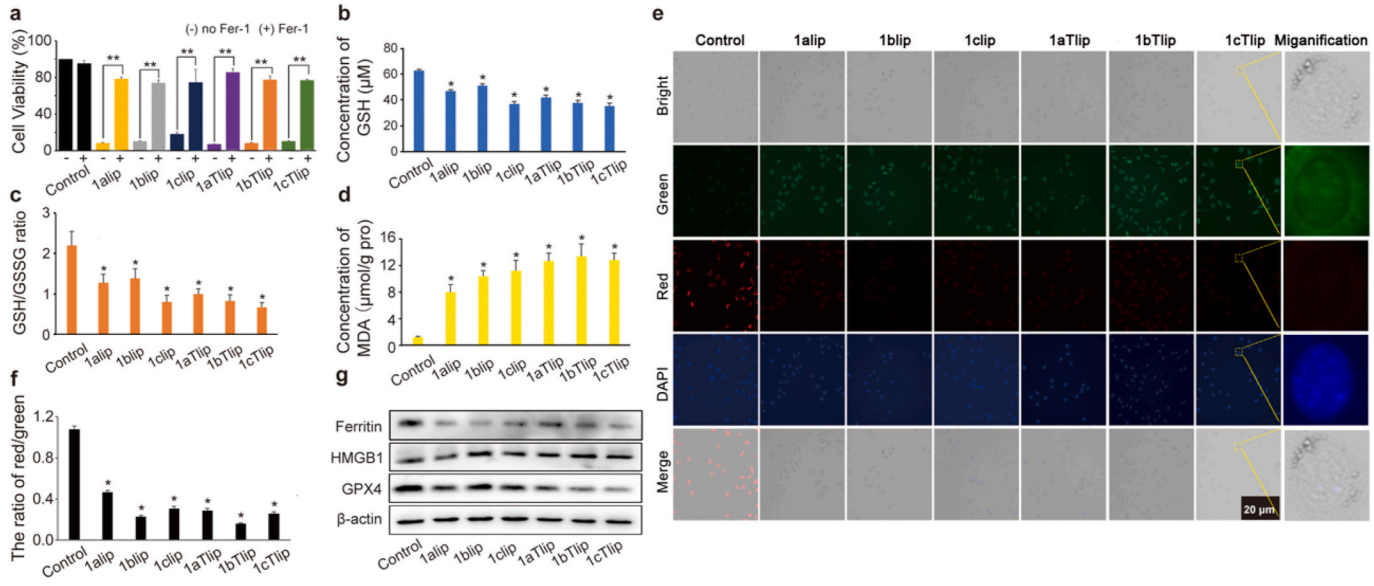

Fig. 6. (a) Cell viability assay. (b and c) assay of GSH content and ratio of GSH versus GSSG. (d) measurement of intracellular MDA levels. (e and f) lipid peroxidation detection while HepG2 cells were stained with C11-BODIPY$^{581/591}$ ($\lambda_{ex} = 581$ nm for red, $\lambda_{ex} = 500$ nm for green), (g) the expression of HMGB1, Ferritin, and GPX4, $^{*}P < 0.05$, $^{**}P < 0.01$. The concentrations of 1a, 1b, 1c, 1alip, 1blip, 1clip, 1aTlip, 1bTlip and 1cTlip are 8.0, 8.6, 17.0, 8.0, 8.6, 17.0, 6.0, 7.3 and 9.7 μM.

increase in HMGB1 content, which further suggested that 1alip, 1blip, 1clip, 1aTlip, 1bTlip, 1cTlip can induce ferroptosis.

2.14. Antitumor activity in vivo

We further explored the effectiveness of 1a, 1alip and 1aTlip on tumor suppression, tissue section and immunohistochemical analysis. Tumor models were successfully established by injecting HepG2 cells suspension into the axillae of BALB/c nude mice. The body weight of mice and volume of tumors were measured daily. As shown in Fig. 7a, the body weight of the nude mice in each group basically maintained a stable growth trend during the treatment period. Meanwhile, no differences in the food consumption, mental status, and physical behavior of the nude mice in each administration group were observed, indicating that 1a, 1alip and 1aTlip have no acute toxicity and relatively safe. Fig. 7b–d described the shape and size of the tumors and relative tumor volume. As can be observed, the tumors in control grew significantly fast, the relative tumor volume in 1a-treated group was slightly smaller than the control, while the growth of tumors was validly inhibited in 1alip and 1aTlip-treated groups. As depicted in Fig. 7e and f, surprisingly, the targeted liposome 1aTlip showed the highest efficacy on preventing the tumor growth, the inhibitory tumor growth rates in 1a, 1alip and 1aTlip-treated groups are 23.24 %, 61.27 % and 76.06 %, respectively. The difference of 1a, 1alip and 1aTlip in the inhibitory

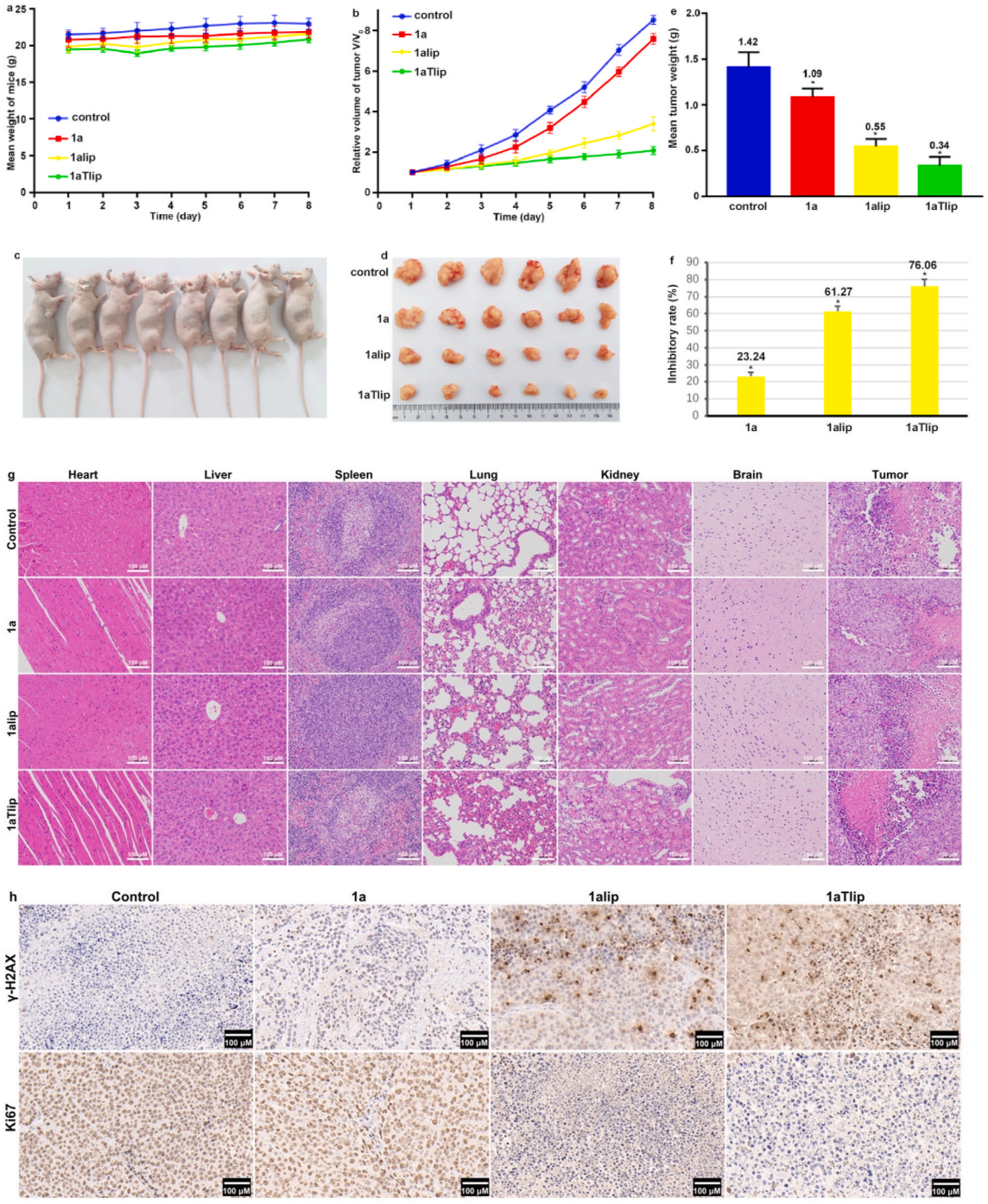

Fig. 7. (a) Weight change curve of mice. (b) Relative tumor volume. (c) BALB/c mouse bearing HepG2 cell tumor. (d) The sizes of tumors. (e and f) The average tumor weight and inhibitory rate (*$P < 0.05$). (g) H&E staining heart, liver, spleen, lung, kidney, brain, and tumor. (h) assays of γ-H2AX and Ki67 in tumor tissues.

tumor growth rate lies in the different cytotoxic activity against HepG2 cells, moreover, the targeted liposome 1aTlip can target the tumor. Taken together, we consider that targeted liposomes bearing targeted head GAlNAc can directly deliver compound 1a to reach the tumor position, and really realize a targetability on inhibiting hepatocellular tumor growth.

Hematoxylin is one of the most used protocols for histopathological analysis of cells and tissues in cancer diagnosis. Observed from Fig. 7g, in the 1a, 1alip and 1aTlip-treated groups, the heart, spleen, liver, kidney, and brain tissues showed no significant changes compared to the blank, However, a small area of alveolar wall was found in the lungs with mild thickening, a small amount of granulocyte infiltration and capillary stasis in the alveolar wall, and mild granular degeneration in the hepatocytes. Additionally, cytoplasmic laxity, nucleus fixation and necrosis and significant increase in cytoplasmic eosinophilia were observed in the tumor tissue.

In addition, we investigated the positive rate of phosphorylated histone H2AX (γ-H2AX) and Ki67 to confirm apoptosis and inhibiting cell proliferation and tumor growth. The positive rate of γ-H2AX reflects the damage degree of DNA [72]. As shown in Fig. 7h, the positive rate in control is 18.9 (±1.4)%. A positive increase of 7.9 % for 1a, 12.5 % for 1alip and 17.2 % for 1aTlip indicated an enhancement of apoptotic cells. Hence, 1alip and 1aTlip cause DNA damage and prevent DNA replication, further induce apoptosis, while 1a displays low apoptotic efficiency, this is consistent with the apoptotic assay. In the assay of ki67, the positive rate in control is 24.7 (±1.5)%, in 1a, 1alip and 1aTlip--treated groups, the positive rates are 18.5 (±1.1), 13.4 (±0.8) and 12.3 (±1.2)%, the decrease in the positive rate shows that 1alip and 1aTlip can validly prevent the cell proliferation and tumor growth. The results demonstrate that 1alip and 1aTlip can inhibit the tumor growth, moreover, 1aTlip shows higher inhibitory efficacy than 1alip under the same experimental conditions.

3. Conclusions

In this study, PIP, NPIP, NNIP and iridium(III) metal compounds 1a, 1b and 1c were synthesized, ordinary 1alip, 1blip, 1clip and the targeted 1aTlip, 1bTlip and 1cTlip were successfully prepared. Compounds 1a, 1b and 1c display low or no cytotoxic activity, while 1alip, 1blip, 1clip and 1aTlip, 1bTlip and 1cTlip show high anticancer activity. The results gained from cell cycle, cell colony and wound healing demonstrate that 1alip-1clip, 1aTlip-1cTlip can validly prevent the cell proliferation in G0/G1 period. Through RNA sequencing studies, we found that 1alip, 1blip, 1clip and 1aTlip, 1bTlip and 1cTlip cause cell death through p53 and PI3K/AKT/mTOR signaling pathways. Additionally, 1alip-1clip, 1aTlip-1cTlip elevate ROS content, lessen mitochondrial membrane potential, result in the mitochondrial dysfunction, further promote Ca^{2+} release. Through activating Beclin-1 protein, promoting the conversion from LC3-I into LC3-II, inducing autophagy. Increase of cell viability (with Fer-1), reduction of GSH, increase of MDA, upregulation of ferritin, HMGB1 and downregulation of GPX4, and C11-BODIPY staining results reveal that 1alip-1clip, 1aTlip-1cTlip can effectively cause ferroptosis. Particularly, antitumor activity in vivo confirms that targeted liposome entrapped compounds 1a displays very high antitumor efficiency with an inhibitory rate of 76.06 % and really realize the targeted liposomes to directly deliver 1a to tumor position. γ-H2AX and ki67 stained results further confirm that 1alip-1clip, 1aTlip-1cTlip can cause apoptosis and inhibit cell proliferation and tumor growth. In summary, we consider that 1alip-1clip, 1aTlip-1cTlip induce HepG2 cell death via four pathways (Fig. 8). In summary, this work can provide help for understanding anticancer mechanism and design and synthesis of iridium(III) compounds as potent anticancer candidate drugs.

4. Experimental

4.1. Materials and methods

The cell bank of Shenzhen (Shenzhen, China) offered human hepatocellular carcinoma SK-Hep1, BEL-7402, HepG2, human normal liver LO2 cells. We purchased 2-phenylpyridine (Hppy), benzaldehyde, 1-nitrobenzaldehyde, 1-nitro-2-naphthalene carboxaldehyde and $IrCl_3{\cdot}3H_2O$ from Beijing HWRK Chem Co. Ltd. Guangzhou Chemical Reagent Factory supplied DMSO and 1,10-phenanthroline (phen). Hydrogenated soybean phospholipids (HSPC), distearoyl phosphatidylglycerol (DSPG-Na) and cholesterol (CHS) were purchased from the Aviator Pharmaceutical Technology Co. Ltd (Shanghai). N-acetylgalactosamine (GalNAc), D-galactosamine (Gal), D-lactitol (D-lactitol) were obtained from Sigma. Through direct injection, HRMS was tested with a Waters Xevo G2-XS QTof mass spectrometer. Using acetone-d_6 as solvent and tetramethylsilane (TMS) as internal standard, NMR spectra

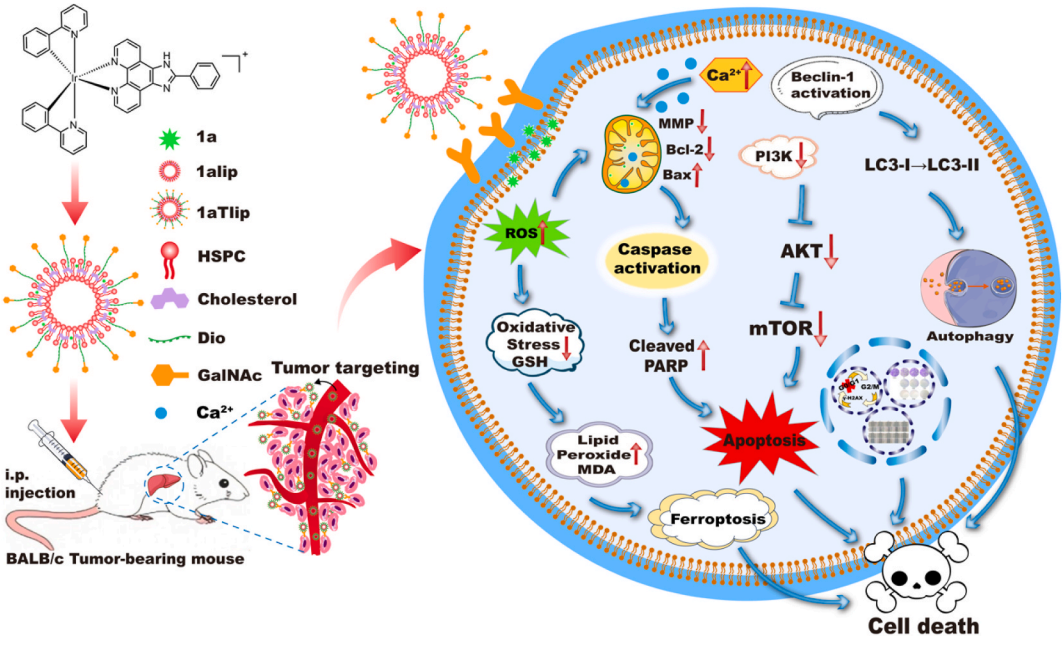

Fig. 8. The mechanism of 1aTlipo inducing HepG2 cell death.

were examined under a Varian-500 spectrometer (500 MHz).

4.2. Preparation of ligands and iridium(III) compounds

4.2.1. Preparation of PIP, NPIP

The ligands PIP and NPIP were prepared as the same method as literature [9,73].

4.2.2. Preparation of NNIP

The mixture of phenanthroline-5,6-dione (0.21 g, 1.0 mmol) [74], 1-nitro-2-naphthaldehyde (0.15 g, 1.0 mmol) and NH_4Ac (1.16 g, 15 mmol) was dissolved in 20 mL of ice acetic acid and refluxed at 130 °C. After 2 h, using concentrated ammonia to neutralize the solution to produce a red precipitate. Yield: 86 %. Anal calcd for $C_{23}H_{13}N_5O_2$: C, 70.58; H, 3.35; N, 17.89 %. Found: C, 70.77; H, 3.16; N, 17.75 %. IR (KBr, cm^{-1}): 3332 w, 3066 w, 1701 w, 1625 w, 1604 w, 1537 s, 1498 w, 1426 m, 1220 m, 1196 m, 1143 m, 1071 s, 1029 s, 864 w, 821 w, 741 w, 661 m, 448 s. HRMS (CH_3OH): m/z = 390.0997 ($[M - H]^-$).

4.2.3. Synthesis of $[Ir(ppy)_2(PIP)](PF_6)$ (1a), $[Ir(ppy)_2(NPIP)](PF_6)$ (1b) and $[Ir(ppy)_2(NNIP)](PF_6)$ (1c)

The precursor *cis*-$[Ir(ppy)_2Cl]_2$ (0.15 mmol, 0.161 g) [75] and PIP (0.30 mmol, 0.086 g), NPIP (0.30 mmol, 0.102 g), NNIP (0.30 mmol, 0.117 g) were dissolved in 30 mL dichloromethane and 15 mL methanol and refluxed at 40 °C under argon, after 7 h, the solution was cooled and added with saturated aqueous NH_4PF_6, then stirred for 2 h, the solution was filtered to obtain yellow filtrate, then removing the solvent, the yellow solid was gained. Through a neutral alumina column with dichloromethane and acetone as eluent, the crude product was purified to obtain yellow powder.

1a: Yield：81 %. Anal cacld for $C_{41}H_{28}N_6PF_6Ir$: C, 52.28; H, 3.00; N, 8.92 %. Found: C, 52.17; H, 3.06; N, 8.81 %. IR (KBr, cm^{-1}): 3373 w, 3040 w, 1658 w, 1607 s, 1562 s, 1548 m, 1226 s, 1163 s, 1103 w, 1076 m, 1063 m, 1030 s, 951 s, 759 s, 703 m, 557 s, 430 s. HRMS (CH_3CN): m/z = 797.1872 ($[M - PF_6)^+$]. ^1H NMR (Acetone-d_6, 500 MHz, Fig. S12, ESI): δ 9.21 (d, J = 8.0 Hz, 2H, $H_{a,a'}$), 8.34 (d, J = 7.5 Hz, 2H, $H_{c,c'}$), 8.28 (d, J = 8.0 Hz, 2H, $H_{1,1'}$), 8.14 (d, J = 5.0 Hz, 2H, $H_{j,n}$), 8.08–8.06 (m, 2H, $H_{7,7'}$), 7.97 (d, J = 7.5 Hz, 2H, $H_{b,b'}$), 7.89 (t, J = 7.5 Hz, 2H, $H_{10,10'}$), 7.65 (t, J = 7.5 Hz, 2H, $H_{8,8'}$), 7.57 (t, J = 7.0 Hz, 1H, H_l), 7.52 (d, J = 5.5 Hz, 2H, $H_{k,m}$), 7.07 (t, J = 7.0 Hz, 2H, $H_{9,9'}$), 7.01–6.95 (m, 4H, $H_{3,3',4,4'}$), 6.31 (d, J = 7.0 Hz, 2H, $H_{2,2'}$). ^{13}C NMR (DMSO-d_6, 125 MHz, Fig. S13, ESI): 167.4 ($C_{5,5'}$), 153.4 ($C_{e,e'}$), 150.9 (C_h), 149.6 ($C_{a,a'}$), 148.8 ($C_{1,1'}$), 144.6 ($C_{6,6'}$), 144.5 (Ci), 139.2 ($C_{c,c',9,9'}$), 132.7 (C_l), 131.7 ($C_{2,2',3,3'}$), 130.8 ($C_{k,m}$), 130.7 ($C_{7,7'}$), 130.0 ($C_{11,11'}$), 129.7 ($C_{10,10'}$), 127.5 ($C_{8,8'}$), 127.1 ($C_{j,n}$), 125.5 ($C_{d,d'}$), 122.8 ($C_{4,4',3,3'}$), 120.4 ($C_{2,2',b,b'}$).

1b: Yield: 83 %. Anal calcd for $C_{41}H_{27}N_7O_2PF_6Ir$: C, 49.90; H, 2.76; N, 9.94 %. Found: C, 49.78; H, 2.86; N, 9.87 %. IR (KBr, cm^{-1}): 3389 w, 3041 w, 1707 w, 1672 w, 1605 s, 1583 s, 1529 s, 1477 m, 1447 s, 1351 s, 1314 m, 1268 s, 1226 m, 1187 w, 1162 m, 1087 s, 1063 s, 1031 s, 844 s, 809 m, 756 s, 669 m, 557 s, 448. HRMS (CH_3CN): m/z = 843.2027 ($[M - PF_6)^+$]. ^1H NMR (Acetone-d_6, 500 MHz, Fig. S14, ESI): δ 8.99 (d, J = 8.5 Hz, 2H, $H_{a,a'}$), 8.27 (d, J = 8.0 Hz, 2H, $H_{1,1'}$), 8.19 (d, J = 8.0 Hz, 1H, H_j)), 8.08 (d, J = 8.0 Hz, 2H, $H_{c,c'}$), 7.99–7.95 (m, 5H, $H_{7,7',b,b',k}$), 7.90–7.86 (m, 3H, $H_{10,10',l}$), 7.71 (s, 1H, H_m), 7.50 (d, J = 6.5 Hz, 2H, $H_{9,9'}$), 7.08–7.04 (m, 2H, $H_{8,8'}$), 7.01–6.98 (m, 4H, $H_{3,3',4,4'}$), 6.31 (dd, J = 1.0, J = 7.5 Hz, 2H, $H_{2,2'}$). ^{13}C NMR (DMSO-d_6, 125 MHz, Fig. S15, ESI): 172.6 ($C_{e,e'}$), 167.5 ($C_{5,5'}$), 151.3 (C_h), 149.5 (C_n), 147.4 ($C_{a,a'}$), 144.6 ($C_{1,1'}$), 143.9 ($C_{6,6'}$), 139.1 ($C_{3,3'}$), 132.7 (C_k), 132.2 (C_j), 131.7 ($C_{c,c'}$), 131.4 (C_l), 130.7 ($C_{8,8',10,10'}$), 126.9 ($C_{7,7',9,9'}$), 125.5 ($C_{11,11'}$), 124.4 (C_i), 124.3 ($C_{d,d'}$), 122.7 ($C_{i,m,g,f}$), 120.4 ($C_{4,4',2,2',b,b'}$).

1c: Yield: 87 %. Anal calcd for $C_{45}H_{29}N_7O_2PF_6Ir$: C, 52.12; H, 2.82; N, 9.46 %. Found: C, 52.33; H, 2.71; N, 9.60 %. IR (KBr, cm^{-1}): 3329 w, 3043 w, 1676 w, 1628 m, 1604 s, 1532 s, 1476 s, 1448 m, 1393 w, 1350 m, 1267 s, 1212 w, 1160 w, 1127 w, 1081 s, 1062 w, 1030 m, 962 w, 854 m, 793 s, 754 s, 556 m, 450 m. HRMS (CH_3CN): m/z = 892.2159 ($[M - PF_6)^+$]. ^1H NMR (Acetone-d_6, 500 MHz, Fig. S16, ESI): δ 8.96 (dd, J = 1.0 Hz, J = 8.0 Hz, 2H, $H_{a,a'}$), 8.71 (d, J = 8.5 Hz, 1H, H_o), 8.26 (d, J = 8.5 Hz, 2H, $H_{1,1'}$), 8.20 (d, J = 8.5 Hz, 1H, H_l), 8.11 (d, J = 8.0 Hz, 1H, H_s), 7.96–7.94 (m, 4H, $H_{c,c',7,7'}$), 7.89–7.86 (m, 4H, $H_{4,4',b,b'}$), 7.74–7.71 (m, 1H, H_m), 7.67–7.62 (m, 2H, $H_{p,q}$), 7.50 (t, J = 8.0 Hz, 2H, $H_{10,10'}$), 7.05 (t, J = 6.0 Hz, 2H, $H_{8,8'}$), 7.01 (t, J = 6.0 Hz, 2H, $H_{9,9'}$), 6.95 (t, J = 7.5 Hz, 2H,$H_{3,3'}$), 6.33 (dd, J = 1.0 Hz, J = 7.5 Hz, 2H, $H_{2,2'}$). ^{13}C NMR (DMSO-d_6, 125 MHz, Fig. S17, ESI): 172.6 ($C_{e,e'}$), 167.5 ($C_{5,5'}$), 167.2 (C_h), 157.1 ($C_{1,1'}$), 151.9 ($C_{a,a'}$), 150.4 ($C_{n,\ 6,6'}$), 149.9 ($C_{3,3'}$), 149.1 (C_k), 146.1 (C_i), 144.8 ($C_{c,c'}$), 144.5 (C_j), 143.4 (C_l), 139.8 (C_o), 138.9 (C_q), 132.6 (C_p), 131.9 (C_8), 131.8 ($C_{8'}$), 130.6 ($C_{10,10'}$), 129.9 (C_s), 129.3 ($_{11,11'}$), 128.7 ($C_{d,d'}$), 127.5 (C_f), 127.1 ($C_{7,7'}$), 126.1 ($C_{9,9'}$), 125.5 (C_4), 125.0 ($C_{4'}$), 124.2 (C_g), 122.6 (C_m), 121.2 ($C_{b,b'}$), 120.3 ($C_{2,2'}$).

4.3. Preparation of targeted liposomes

3,6-dioxo-divinyloctanedioic acid (Dio), 5-cholesten-3b-ol-3,6-dioxo-vinyloctanedioate (CHS-Dio) and a targeted ASGP-r receptor glycoligand molecule (CHS-Dio-6-GalNAc) were prepared based on the literature [76]. Through a thin film dispersion method, the targeted liposomes encapsulated 1a, 1b and 1c were obtained via the following procedures: (I) 40 mg of hydrogenated soy phosphatide (HSPC), 10 mg of cholesterol (CHS), 4 mg of distearoyl phosphatidylglycerol (DSPG-Na), 2 mg of 1a, 1b, 1c, 6.5 mg of CHS-PEG_2-6-GalNAc together were placed in a round-bottom flask and mixed thoroughly. (II) dissolve the above mixture in chloroform, heated at 55 °C in a water bath and a lipid film was formed. (III) 10 mL distilled water was added into the dried lipid film, then heating at 55 °C for 1 h. (IV) The suspension of the liposome was ultrasonicated (ultrasonic cell milling machine, Sciente-IID, China) for 10 min. (V) homogenization was performed two times at 90 MPa and three times at 180 MPa, respectively. (VI) the samples were finally stored at 4 °C.

The ordinary liposome entrapped iridium(III) compounds 1alip, 1blip and 1clip were prepared with the same method described for the targeted liposomes without CHS-PEG_2-6-GalNAc.

4.4. Encapsulation rate determination

The encapsulation rate (EE%) was determined by UV–Vis spectra based on the following procedures: (A) Standard curve of absorbance versus compound concentration: (I) 10 mg 1a, 1b and 1c compounds were dissolved in anhydrous ethanol to obtain 1 mg mL^{-1} solution. (II) 0.5, 0.75, 1.0, 1.25, 1.5, 2.0 mL of 1 mg mL^{-1} solutions were diluted with anhydrous ethanol to gain a concentration of 5, 7.5, 10, 12.5, 15 and 20 mg mL^{-1} solution (5 mL). (III) Determine the maximum absorbance values, then plot the standard curve (concentration versus absorbance value). (B) (I) 1 mL of liposomes were placed in 10 mL of volumetric bottle and diluted with absolute ethanol to prepare 10 mL solution. (II) Liposomes breakage: 10 mL solution was dissolved in anhydrous ethanol at 25 °C for 3 h, then filtered through a microporous membrane (0.22 μm diameter). (III) By UV–Vis spectroscope, determine the maximum absorbance values. (IV) The concentration of compounds 1a, 1b and 1c was calculated based on the obtained standard curve. (V) The encapsulation efficiency (EE) values were gained via the following equation:

$$EE\% = \frac{C_{drug}}{T_{drug}} \times 100\%$$

where C_{drug} stands for the concentration of the compounds entrapped in the liposome, T_{drug} represents total concentration of the compounds.

4.5. Examination of particle size, zeta potential and stability

The mean particle size and zeta potential of ordinary liposome or targeted liposome entrapped compounds were detected in a nano-particle size analyzer (Beckman coulter). According to the literature [77], through UV–Vis spectra, the stability of the compounds, ordinary and targeted liposome encapsulated compounds was examined at 0 and 48 h in PBS solution. The purity of 1a, 1b, 1c was measured by HPLC (mobile phases I: H_2O and 0.1 % trifluoroacetic; II methanol and 0.1 % trifluoroacetic acid).

4.6. Determination of lipid-water partition coefficient (logP)

In organic (*n*-octanol) and H_2O phases, the distribution of compounds 1a-1c was measured by the shaking bottle method [78]. In brief, 2 mg of compounds of 1a, 1b or 1c was dissolved in 2 mL octanol and 2 mL H_2O, the mixed solutions were consecutively shaken for 30 h at 37 °C. Thereafter, the organic and water phases were separated through 15 min of centrifugation (1000 rpm). The concentrations (C_o) of the compounds 1a-1c in organic phase were examined using UV–Vis spectra. The mean lipid-water partition coefficient $\log P = \log(C_o/C_w)$.

4.7. Detection of pK_a values

80 mM HCl, 50 mM KOH and 50 μM compounds 1a, 1b, 1c were prepared with CH_3CN and double distilled H_2O (*v*/v, 4:6). The pK_a values of 1a, 1b and 1c were measured using potentiometric titration method. Through gradually titrating the compound solution with HCl to reduce pH to 2.0. After that, the above solutions were slowly titrated with KOH solution, the pH values were recorded, the pK_a values were gained according to the curve of pH value versus the volumes of KOH solution.

4.8. In vitro anti-cancer activity assay

The anti-cancer activities of compounds and liposome encapsulated compounds against BEL-7402, HepG2, SK-Hep1 and LO2 cells were assessed by 3-(4,5-dimethylthiazole-2-yl)-2,5-diphenyltetrazolium bromide (MTT) method [79]. The cells were incubated with six different concentration of compounds 1a, 1b, 1c, 1alip, 1blip, 1clip, 1aTlip, 1bTlip and 1cTlip dissolved in DMSO (less than 0.05 %) for 48 h, then the cells were dyed with 10 % MTT dye for 6 h, 100 μL DMSO was added to dissolve the purple formazan product. Ultimately, we recorded the absorbance values at 490 nm.

4.9. Measurement of cellular uptake

In brief, in 12-well plates, HepG2 cells were cultivated overnight. After 6 h of incubation of HepG2 cells with IC_{50} values of 1a, 1b, 1c, 1alip, 1blip, 1clip, 1aTlip, 1bTlip and 1cTlip, HepG2 cells were washed several times to eliminate the remaining compounds. Ultimately, HepG2 cells were immediately observed.

4.10. Cell colony, cell migration research

(a) cell colony: HepG2 cells growing in 6-well plate were cultured with 1a, 1b, 1c, 1alip, 1blip, 1clip, 1aTlip, 1bTlip and 1cTlip at IC_{50} concentration for a week. During this period, the culture medium was replaced every day. Finally, we used paraformaldehyde to fix the cells and applied crystal violet to dye the cells and photographed. (b) cell migration: At 37 °C, HepG2 (1×10^4 cells/well) were cultivated in 6-well plate, after the cell density reached about 75 %, using the pipette tip to draw two straight lines to construct artificial wound area. PBS buffer solution was used to wash dead cells away. IC_{50} concentration of compounds 1a, 1b, 1c, 1alip, 1blip, 1clip, 1aTlip, 1bTlip and 1cTlip were used to treat the wells for 24 h, and the degree of wound healing was observed under a microscope at 0 and 24 h.

4.11. Ca^{2+} concentration determination

IC_{50} concentrations of 1a, 1b, 1c, 1alip, 1blip, 1clip, 1aTlip, 1bTlip and 1cTlip were used to treat HepG2 cells for 24 h. After washing and centrifugation, cells were stained with Fluo-3-pentaacetoxymethyl ester (Flu-3 AM) and intracellular Ca^{2+} content was examined by flow cytometry.

4.12. Cell cycle arrest

Placing HepG2 cells in 6-well plate and grown for 20 h, cells were co-incubated for 24 h with IC_{50} concentration of 1a, 1b, 1c, 1alip, 1blip, 1clip, 1aTlip, 1bTlip and 1cTlip, washing three times, cells were collected, lysed, and fixed with 75 % ethanol for 15 h. Then cells were discolored with 0.2 % Triton X-100, 15 μL 1 mg mL^{-1} PI and 15 μL 1 mg mL^{-1} RNase for 20 min and analyzed under a flow cytometry.

4.13. Apoptosis studies

1×10^5 cells/well of HepG2 cells were seeded into 6-well plate in the incubator at 37 °C, 5 % of CO_2 overnight. Then the cells were exposed to IC_{50} of 1a, 1b, 1c, 1alip, 1blip, 1clip, 1aTlip, 1bTlip and 1cTlip. After a day, washing cells three times, staining cells 25 min using propidium iodide (PI) and Annexin V-FITC. Finally, the cells were analyzed under a flow cytometer.

4.14. Quantitative assay of intracellular ROS

Placing HepG2 cells into 6-well plate and incubated for 20 h. IC_{50} of 1a, 1b, 1c, 1alip, 1blip, 1clip, 1aTlip, 1bTlip and 1cTlip were added to the cells, after 24 h, washing cells four times, using 15 μM 2′,7′-dichlorodihydrofluorescein diacetate to stain the cells for 25 min, ROS content was examined.

4.15. Ferroptosis studies

(I) Ferrotin-1 assay for cell viability

HepG2 cells were treated with the following nineteen groups: ferrotin-1 (Fer-1), IC_{50} concentrations of 1a, 1a + Fer-1; 1b, 1b + Fer-1; 1c, 1c + Fer-1; 1alip, 1alip + Fer-1; 1blip, 1blip + Fer-1; 1clip, 1clip + Fer-1; 1aTlip, 1aTlip + Fer-1; 1bTlip, 1bTlip + Fer-1; 1cTlip, 1cTlip + Fer-1. After 36 h, 10 % MTT dye was added to the cells for 6 h, then we applied 100 μL DMSO to dissolve the purple formazan. Ultimately, we determined the absorbance values (490 nm).

(II) Determination of GSH and MDA content
  (a) glutathione (GSH) content: HepG2 cells were cultivated into 6-well plate for 20 h, a treatment of 24 h of HepG2 cells with compounds 1a, 1b, 1c, 1alip, 1blip, 1clip, 1aTlip, 1bTlip and 1cTlip (IC_{50} concentration) at 37 °C with 5 % CO_2, the cells were collected by lysis, then we determined the contents of total glutathione and oxidized glutathione disulfide (GSSG). (b) According to the method described in the literature [73], we also examined MDA content.

(III) Lipid peroxidation studies

HepG2 cells were seeded in 6-well plate for 20 h, the cells were incubated with 1alip, 1blip, 1clip, 1aTlip, 1bTlip, 1clip (IC_{50} concentration) for 24 h, then the cells were washed three times and dyed with C11-BODIPY for 30 min and photographed. The red and green fluorescence were examined using flow cytometry.

4.16. Assay of protein expression

The assay of protein expression was performed via the following ten steps: (a) HepG2 cells were spread evenly overnight in DMEM containing 10 % FBS. (b) HepG2 cells were cultivated with IC_{50} value of 1a, 1b, 1c, 1alip, 1blip, 1clip, 1aTlip, 1bTlip and 1cTlip for 24 h, the culture fluid was dismissed, and the cells were lysed and collected in 1.5 mL EP tubes. (c) The cells were centrifuged (12,000 rpm, 13 min) and the supernatant was collected in a new 1.5 mL EP tube. (d) Concentration of protein was examined based on BCA Protein Concentration Assay Kit. (e) Protein from individual sample was added to every lane, sodium dodecyl sulfate-polyacrylamide gel electrophoresis was carried out for 2 h. (f) The observed protein bands were transferred to polyvinylidene difluoride (PVDF) membranes, the bands were blocked for 1 h with 5 % skimmed milk. (VII) After removal of the blocking solution, using TBST solution to wash the strips four times, incubated with the primary antibody overnight at 4 °C. (g) On the second day, remove the primary antibody, using TBST to wash the membrane four times. (h) The secondary antibody was used to co-incubate the membrane for 75 min. (i) ECL chemiluminescence reagent was added and the bands were observed under an Amersham ECL (electrochemiluminescence) kit (Bainite Biotechnology, China).

4.17. RNA sequencing (RNA-seq) studies

After 24 h treatment of HepG2 cells with $2 \times IC_{50}$ values of 1alip and 1aTlip, washing the cells three times with PBS solution (containing DEPC), adding 350 μL of RNA extract solution to each well, the cells were lysed, using Trizol reagent to separate the total RNA. The sequencing libraries were constructed based on the TruSeq RNA sample preparation kit. Then the library fragments were purified and quantified. Ultimately, on the Hiseq platform (illumine), the sequencing library was sequenced.

4.18. Co-location and studies on change of mitochondrial membrane potential

(I) Co-location assays

The co-location of the compounds at mitochondria was investigated. HepG2 cells were co-cultivated with 1a, 1b, 1c, 1alip, 1blip, 1clip, 1aTlip, 1bTlip and 1cTlip (IC_{50} concentration) for 6 h, washing the cells three times, using MitoTracker Deep Red (ThermoFisher 15 nM) to stain the cells for 15 min at room temperature, finally, HepG2 cells were photographed.

(II) Examination of change in mitochondrial membrane potential

Use IC_{50} values of 1a, 1b, 1c, 1alip, 1blip, 1clip, 1aTlip, 1bTlip and 1cTlip to treat HepG2 cells for 24 h, then washing the cells three times, the cells were discolored with 5,5′-6,6′-tetrachloro-1,1′-3,3′-tetrethylbenzimidalylcarbocyanine iodide (JC-1), ultimately, the cells were observed. The green fluorescence intensity was quantitatively measured according to the literature [17].

4.19. In vivo anti-tumor efficacy

Guangdong Province Animal Centre supplied nude mice, all experimental procedures abided by the rules and regulations drawn up by Animal Ethics Committee of Guangdong Pharmaceutical University. In the assay of in vivo anti-tumor activity, HepG2 cells were transplanted into armpit of BALB/c nude mice, then dividing casually the mice bearing tumor into four groups: blank, 2.67 mg kg^{-1} of 1a, 1alip and 1aTlip ($n = 6$). When tumor diameter attains 5 mm, the mice were injected saline, 2.67 mg kg^{-1} 1a, 2.67 mg kg^{-1} 1alip and 2.67 mg kg^{-1} 1aTlip for consecutively seven days. During total experiments, we recorded the weight and the tumor volume every day. The tumors were separated on the 8th day, the inhibitory tumor growth rate was calculated according to the equation:

$$[(M_1 - M_2) / M_1] \times 100\%$$

M_1 and M_2 represent mean tumor weight in blank and drug-treated groups.

4.20. Drug toxicity test

From the different groups, we randomly selected tumor tissues of brain, kidney, lung, heart, liver, spleen. These tissues were washed with 0.9 % saline and then frozen in paraformaldehyde for 24 h. After fixation, soaking the tissues in paraffin, then the tissues were cut into slices (5 mm), hematoxylin (H&E) was applied to dye the slices at room temperature.

CRediT authorship contribution statement

Jing Chen: Investigation, Methodology, Writing – original draft. **Wenlong Li:** Investigation, Methodology. **Gechang Li:** Data curation, Software. **Xiaoming Liu:** Investigation. **Chunxia Huang:** Data curation. **Hua Nie:** Methodology, Project administration. **Lijuan Liang:** Formal analysis. **Yi Wang:** Software. **Yunjun Liu:** Conceptualization, Funding acquisition, Project administration, Supervision, Writing – review & editing.

Declaration of competing interest

Authors declare no competing interest exists.

Data availability

The data that has been used is confidential.

Acknowledgements

This research was supported by the National Natural Science Foundation of China (No. 21877018).

Appendix A. Supplementary data

Supplementary data to this article can be found online at https://doi.org/10.1016/j.ejmech.2023.116078.

References

[1] X.D. Song, X. Kong, S.F. He, J.X. Chen, J. Sun, B.B. Chen, J.W. Zhao, Z.W. Mao, Cyclometalated iridium(III)-guanidinium complexes as mitochondria-targeted anticancer agents, Eur. J. Med. Chem. 138 (2017) 246–254.
[2] T.F. Yang, M.H. Zhu, M. Jiang, F. Yang, Z.L. Zhang, Current status of iridium-based complexes against lung cancer, Front. Pharmacol. 13 (2022), 1025544.
[3] M.X. Shao, M.M. Yao, X.C. Liu, C. Gao, W.Y. Liu, J.H. Guo, J.W. Zong, X.Z. Sun, Z. Liu, In vitro and in vivo of triphenylamine-appended fluorescent half-sandwich iridium(III) thiosemicarbazones antitumor complexes, Inorg. Chem. 60 (2021) 17063–17073.
[4] R.X. Xu, Y.T. Wu, Z. Liu, J.F. Liu, X.C. Liu, Lysosomal targeted cyclometallic iridium(iii) salicylaldehyde-coumarin schiff base complexes and anticancer application, Front. Chem. 10 (2022), 906954.
[5] Z.H. Wang, Z.X. Lv, X.C. Liu, Y.T. Wu, J.Y. Chang, R.X. Dong, C.Y. Li, X.A. Yuan, Z. Liu, Anticancer application of ferrocene appended configuration-regulated half-sandwich iridium(iii) pyridine complexes, J. Inorg. Biochem. 237 (2022), 112010.
[6] C. Huang, C. Liang, T. Sadhukhan, S. Banerjee, Z.X. Fan, T.X. Li, Z.L. Zhu, P. Y. Zhang, K. Raghavachari, H.Y. Huang, In-vitro and in-vivo photocatalytic cancer therapy with biocompatible iridium(III) photocatalysts, Angew. Chem. Int. Ed. 60 (2021) 9474–9479.
[7] H.W. Zhang, X.F. Liao, X.Y. Wu, C.L. Shi, Y.Y. Zhang, Y.H. Yuan, W.L. Li, J. W. Wang, Y.J. Liu, iridium(III) complexes entrapped in liposomes trigger mitochondria-mediated apoptosis and gsdme-mediated pyroptosis, J. Inorg. Biochem. 228 (2022), 111706.

[8] W.W. Qin, Z.Y. Pan, D.H. Cai, Y. Li, L. He, Cyclometalated iridium(III) complexes for mitochondria-targeted combined chemo-photodynamic therapy, Dalton Trans. 49 (2020) 3562–3569.

[9] Y.H. Yuan, C.L. Shi, X.Y. Wu, W.L. Li, C.X. Huang, L.J. Liang, J. Chen, Y. Wang, Y. J. Liu, Synthesis and anticancer activity in vitro and in vivo evaluation of iridium (III) complexes on mouse melanoma b16 cells, J. Inorg. Biochem. 232 (2022), 111820.

[10] J. Zhao, Y. Gao, W.Y. He, W. Wang, W.W. Hu, Y.Y. Sun, Synthesis, characterization and biological evaluation of two cyclometalated iridium(III) complexes containing a glutathione s-transferase inhibitor, J. Inorg. Biochem. 238 (2023), 112050.

[11] G. Gupta, S. Cherukommu, G. Srinivas, S.W. Lee, S.H. Mun, J. Jung, N. Nagesh, C. Y. Lee, Bodipy-based Ru(II) and Ir(III) organometallic complexes of avobenzone, a sunscreen material: potent anticancer agents, J. Inorg. Biochem. 189 (2018) 17–29.

[12] W.G. Chen, X.H. Cai, Q. Sun, X.H. Guo, C.M. Liang, H. Tang, H.M. Huang, H. Luo, L.M. Chen, J.C. Chen, Design and synthesis of aptamer-cyclometalated iridium (III) complex conjugate targeting cancer cells, Eur. J. Med. Chem. 236 (2022), 114335.

[13] G. Gupta, P. Kumari, J.Y. Ryu, J. Lee, S.M. Mobin, C.Y. Lee, Mitochondrial localization of highly fluorescent and photostable bodipy-based ruthenium(II), rhodium(III), and iridium(III) metal complexes, Inorg. Chem. 58 (2019) 8587–8595.

[14] B. Tang, D. Wan, Y.J. Wang, Q.Y. Yi, B.H. Guo, Y.J. Liu, An iridium (iii) complex as potent anticancer agent induces apoptosis and autophagy in b16 cells through inhibition of the akt/mtor pathway, Eur. J. Med. Chem. 145 (2018) 302–314.

[15] G. Ludwig, S. Mijatović, I. Ranđelović, M. Bulatović, D. Miljković, D. Maksimović-Ivanić, M. Korb, H. Lang, D. Steinborn, G.N. Kaluđerović, Biological activity of neutral and cationic iridium(III) complexes with κP and κP,κS coordinated $Ph_2PCH_2S(O)_xPh$ (x = 0-2) ligands, Eur. J. Med. Chem. 69 (2013) 216–222.

[16] X.C. Liu, Z. Wang, X.R. Zhang, X.C. Lv, Y. Song, R.X. Dong, G.X. Li, X.Y. Ren, Z. Y. Ji, X.A. Yuan, Z. Liu, Configurationally regulated half-sandwich iridium(III)-ferrocene heteronuclear metal complexes: potential anticancer agents, J. Inorg. Biochem. 249 (2023), 112393.

[17] Y.H. Yuan, Y.Y. Zhang, J. Chen, C.X. Huang, H.M. Liu, W.L. Li, L.J. Liang, Y. Wang, Y.J. Liu, Synthesis, biological evaluation of novel iridium(III) complexes targeting mitochondria toward melanoma b16 cells, Eur. J. Med. Chem. 247 (2023), 115046.

[18] J. Chen, H.M. Liu, Y.C. Chen, H.Y. Hu, C.X. Huang, Y. Wang, L.J. Liang, Y.J. Liu, Iridium(III) complexes inhibit the proliferation and migration of bel-7402 cells through the pi3k/akt/mtor signaling pathway, J. Inorg. Biochem. 241 (2023), 112145.

[19] S.Y. Guo, F.M. Wei, J. Karges, Y.K. Zhao, L.N. Ji, H. Chao, Cancer cell membrane-camouflaged and h2o2-activatable nanocomposites for synergistic chemotherapy and two-photon photodynamic therapy against melanoma, Inorg. Chem. Front. 10 (2023) 2716–2730.

[20] J. Bonelli, E. Ortega-Forte, G. Vigueras, M. Bosch, N. Cutillas, J. Rocas, J. Ruiz, V. Marchán, Polyurethane-polyurea hybrid nanocapsules as efficient delivery systems of anticancer Ir(III) metallodrugs, Inorg. Chem. Front. 9 (2022) 2123–2138.

[21] M. Zhong, J. He, B.X. Zhang, Q. Liu, J.G. Fang, Mitochondria-targeted iridium-based photosensitizers enhancing photodynamic therapy effect by disturbing cellular redox balance, Free Radic. Biol. Med. 195 (2023) 121–131.

[22] Q. Sun, Y. Wang, Q.X. Fu, A. Ouyang, S.H. Liu, Z.Y. Wang, Z.J. Su, J.X. Song, Q. L. Zhang, P.Y. Zhang, D.S. Lu, Sulfur-coordinated organoiridium(III) complexes exert breast anticancer activity via inhibition of wnt/β-catenin signaling, Angew. Chem. Int. Ed. 60 (2021) 4841–4848.

[23] Q.Y. Yi, D. Wan, B. Tang, Y.J. Wang, W.Y. Zhang, F. Du, M. He, Y.J. Liu, Synthesis, characterization and anticancer activity in vitro and in vivo evaluation of an iridium (III) polypyridyl complex, Eur. J. Med. Chem. 145 (2018) 338–349.

[24] X.Y. Zhao, J.Y. Zhang, W. Zhang, Z.J. Guo, W. Wei, X.X. Wang, J. Zhao, A chiral fluorescent ir(III) complex that targets the GPX4 and ErbB pathways to induce cellular ferroptosis, Chem. Sci. 14 (2023) 1114–1122.

[25] W.J. Wang, Y.Y. Ling, Y.M. Zhong, Z.Y. Li, C.P. Tan, Z.W. Mao, Ferroptosis-enhanced cancer immunity by a ferrocene-appended iridium(III) diphosphine complex, Angew. Chem., Int. Ed. 61 (2022).

[26] Y. Li, C.P. Tan, W. Zhang, L. He, L.N. Ji, Z.W. Mao, Phosphorescent iridium(III)-bis-N-heterocyclic carbene complexes as mitochondria-targeted theranostic and photodynamic anticancer agents, Biomaterials 39 (2015) 95–104.

[27] C.C. Liao, D.Q. Xu, X.O. Liu, Y.Q. Fang, J. Yi, X.F. Li, B.H. Guo, Iridium (iii) complex-loaded liposomes as a drug delivery system for lung cancer through mitochondrial dysfunction, Int. J. Nanomed. 13 (2018) 4417–4431.

[28] M. Fandzloch, A. Jaromin, M. Zaremba-Czogalla, A. Wojtczak, A. Lewińska, J. Sitkowski, J. Wiśniewska, I. Łakomska, J. Gubernator, Nanoencapsulation of a ruthenium(ii) complex with triazolopyrimidine in liposomes as a tool for improving its anticancer activity against melanoma cell lines, Dalton Trans. 49 (2020) 1207–1219.

[29] Y.Y. Gu, L. Bai, Y.Y. Zhang, H.W. Zhang, D.G. Xing, L. Tian, Y. Zhou, J. Hao, Y. J. Liu, Liposome as drug delivery system enhance anticancer activity of iridium (III) complex, J. Liposome Res. 31 (2021) 342–355.

[30] A. D Souza Anisha, P.V. Devarajan, Asialoglycoprotein Receptor Mediated Hepatocyte Targeting – Strategies and Applications, J. Control. Release, 2015.

[31] X.G. Huang, J. Leroux, B. Castagner, Well-defined multivalent ligands for hepatocytes targeting via asialoglycoprotein receptor, Bioconjugate Chem. 28 (2017) 283–295.

[32] A.N. Zelensky, J.E. Gready, The c-type lectin-like domain superfamily, FEBS J. 272 (2005) 6179–6217.

[33] H. Nie, B. Qiu, Q.X. Yang, Y. Zhao, X.M. Liu, Y.T. Zhang, F.L. Liao, S.Y. Zhang, Effect of gal/GalNAc regioisomerism in galactosylated liposomes on asialoglycoprotein receptor-mediated hepatocyte-selective targeting in vivo, J. Liposome Res. 31 (2021) 79–89.

[34] T.M. Allen, P.R. Cullis, Liposomal drug delivery systems: from concept to clinical applications, Adv. Drug Deliv. Rev. 65 (2013) 36–48.

[35] S. Shah, V. Dhawan, R. Holm, M.S. Nagarsenker, Y. Perrie, Liposomes: advancements and innovation in the manufacturing process, Adv. Drug Deliv. Rev. 154–155 (2020) 102–122.

[36] L.E. Gerweck, S.V. Kozin, S.J. Stocks, The pH partition theory predicts the accumulation and toxicity of doxorubicin in normal and low-pH-adapted cells, Br. J. Cancer 79 (1999) 838–842.

[37] M. Jacobs, Some aspects of cell permeability to weak electrolytes, Cold Spring Harbor Symp. Quant. Biol. 8 (1940) 30–49.

[38] B.P. Mahoney, N. Raghunand, B. Baggett, R.J. Gillies, Tumor acidity, ion trapping and chemotherapeutics, Biochem. Pharmacol. 66 (2003) 1207–1218.

[39] D.J. Adams, L.R. Morgan, Tumor physiology and charge dynamics of anticancer drugs: implications for camptothecin-based drug development, Curr. Med. Chem. 18 (2011) 1367–1372.

[40] D.T. Manallack, The pKa distribution of drugs: application to drug discovery, J. Med. Chem. 1 (2007) 25–38.

[41] Y.C. Chen, Y.Y. Gu, H.Y. Hu, H.M. Liu, W.L. Li, C.X. Huang, J. Chen, L.J. Liang, Y. J. Liu, Design, synthesis and biological evaluation of liposome entrapped iridium (iii) complexes toward SGC-7901 cells, J. Inorg. Biochem. 241 (2023), 112134.

[42] H. Mao, L.N. Zhang, Y.M. Yang, J.T. Sun, B.P. Deng, J.B. Feng, Q.Q. Shao, A. L. Feng, B.F. Song, X. Qu, Rhobtb2 (DBC2) functions as tumor suppressor via inhibiting proliferation, preventing colony formation and inducing apoptosis in breast cancer cells, Gene 486 (2011) 74–80.

[43] T.B. Deramaudt, D. Dujardin, F. Noulet, S. Martin, R. Vauchelles, K. Takeda, P. Ronde, Altering FAK-paxillin interactions reduces adhesion, migration and invasion processes, PLoS One 9 (2014), e92059.

[44] K.H. Ren, H.X. Jin, C.J. Bian, H.W. He, X. Liu, S.H. Zhang, Y.G. Wang, R.G. Shao, Mr-1 modulates proliferation and migration of human hepatoma HepG2 cells through myosin light chains-2 (MCL2)/focal adhesion kinase (FAK)/Akt signaling pathway, J. Biol. Chem. 283 (2008) 35598–35605.

[45] X.Z. Chen, Z.Y. Cao, T.S. Chen, Y.Q. Zhang, Z.Z. Liu, Y.T. Su, L.M. Liao, J. Du, Water extract of hedyotis diffusa willd suppresses proliferation of human HepG2 cells and potentiates the anticancer efficacy of low-dose 5-fluorouracil by inhibiting the CDK2-E2F1 pathway, Oncol. Rep. 28 (2012) 742–748.

[46] H.W. Zhao, Y.B. Zhang, J.M. Sun, C. Zhan, L. Zhao, Raltitrexed inhibits hepg2 cell proliferation via G0/G1 cell cycle arrest, Oncol. Res. 23 (2016) 237–248.

[47] Y. Sun, Y. Liu, X.L. Ma, H. Hu, The influence of cell cycle regulation on chemotherapy, Int. J. Mol. Sci. 22 (2021) 6923.

[48] P. Singh, B. Lim, Targeting apoptosis in cancer, Curr. Oncol. Rep. 24 (2022) 273–284.

[49] J.W. Wang, H.M. Liu, X.Y. Wu, C.L. Shi, W.L. Li, Y.H. Yuan, Y.J. Liu, D.G. Xing, Induction of apoptosis in SGC-7901 cells by iridium(III) complexes via endoplasmic reticulum stress-mitochondrial dysfunction pathway, J. Biol. Inorg. Chem. 27 (2022) 455–469.

[50] G. Koopman, C.P.M. Reutelingsperger, G.A.M. Kuijten, R.M.J. Keehnen, S.T. Pals, M.H.J. van Oers, Annexin v for flow cytometric detection of phosphatidylserine expression on b cells undergoing apoptosis, Blood 84 (1994) 1415–1420.

[51] E.M. Bruckheimer, S.H. Cho, M. Sarkiss, J. Herrmann, T.J. McDonnell, The Bcl-2 gene family and apoptosis, Adv. Biochem. Eng. Biot. (1998) 75–105.

[52] X. Li, F. Fang, Y. Gao, G. Tang, W.Q. Xu, Y.H. Wang, R.X. Kong, A. Tuyihong, Z. C. Wang, Ros induced by killerred targeting mitochondria (MTKR) enhances apoptosis caused by radiation via cyt c/caspase-3 pathway, Oxid. Med. Cell. Longev. (2019) 1–11, 2019.

[53] Y. Peng, Y.Y. Wang, C. Zhou, W.X. Mei, C.C. Zeng, PI3K/Akt/mTOR pathway and its role in cancer therapeutics: are we making headway? Front. In. Oncol. 12 (2022), 819128.

[54] E.J. Sun, M. Wankell, P. Palamuthusingam, C. McFarlane, L. Hebbard, Targeting the PI3K/Akt/mTOR pathway in hepatocellular carcinoma, Biomed 9 (2021) 1639.

[55] R.J. Sun, R.R. Zhai, C.L. Ma, W. Miao, Combination of aloin and metformin enhances the antitumor effect by inhibiting the growth and invasion and inducing apoptosis and autophagy in hepatocellular carcinoma through PI3K/AKT/mTOR pathway, Cancer Med. 9 (2020) 1141–1151.

[56] A.K. Maurya, M. Vinayak, PI-103 attenuates PI3K-AKT signaling and induces apoptosis in murinet-cell lymphoma, Leuk. Lymphoma 58 (2017) 1153–1161.

[57] S.Y. Choi, F. Gonzalvez, G.M. Jenkins, C. Slomianny, D. Chretien, D. Arnoult, P. X. Petit, M.A. Frohman, Cardiolipin deficiency releases cytochrome c from the inner mitochondrial membrane and accelerates stimuli-elicited apoptosis, Cell Death Differ. 14 (2007) 597–606.

[58] L.V. Loftus, S.R. Amend, K.J. Pienta, Interplay between cell death and cell proliferation reveals new strategies for cancer therapy, Int. J. Mol. Sci. 23 (2022) 4723.

[59] L.J. Su, J.H. Zhang, H. Gomez, R. Murugan, X. Hong, D.X. Xu, F. Jiang, Z.Y. Peng, Reactive oxygen species-induced lipid peroxidation in apoptosis, autophagy, and ferroptosis, Oxid. Med. Cell. Longev. (2019), 5080843, 2019.

[60] S. Tran, W.D. Fairlie, E.F. Lee, Beclin1: protein structure, function and regulation, Cells 10 (2021) 1522.

[61] C. Pena-Martinez, A.D. Rickman, B.L. Heckmann, Beyond autophagy: lc3-associated phagocytosis and endocytosis, Sci. Adv. 8 (2022) n1702.

[62] P.F. Liu, Y.T. Feng, H.W. Li, X. Chen, G.S. Wang, S.Y. Xu, Y.L. Li, L. Zhao, Ferrostatin-1 alleviates lipopolysaccharide-induced acute lung injury via inhibiting ferroptosis, Cell. Mol. Biol. Lett. 25 (2020) 1–14.

[63] H.J. Forman, H.Q. Zhang, A. Rinna, Glutathione: overview of its protective roles, measurement, and biosynthesis, Mol. Aspect. Med. 30 (2009) 1–12.

[64] J.M. Estrela, A. Ortega, E. Obrador, Glutathione in cancer biology and therapy, Crit. Rev. Clin. Lab Sci. 43 (2008) 143–181.
[65] M. Jelic, A. Mandic, S. Maricic, B. Srdjenovic, Oxidative stress and its role in cancer, J. Cancer Res. Therapeut. 17 (2021) 22.
[66] X.C. Li, J.Y. Zeng, Y.P. Liu, M.S. Liang, Q.R. Liu, Z. Li, X.J. Zhao, D.F. Chen, Inhibitory effect and mechanism of action of quercetin and quercetin diels-alder anti-dimer on erastin-induced ferroptosis in bone marrow-derived mesenchymal stem cells, Antioxidants 9 (2020) 205.
[67] H. Yuk, M. Abdullah, D. Kim, H. Lee, S. Lee, Necrostatin-1 prevents ferroptosis in a RIPK1- and Ido-independent manner in hepatocellular carcinoma, Antioxidants 10 (2021) 1347.
[68] H. Dong, Z.Z. Qiang, D.D. Chai, J.L. Peng, Y.Y. Xia, R. Hu, H. Jiang, Nrf2 inhibits ferroptosis and protects against acute lung injury due to intestinal ischemia reperfusion via regulating SLC7A11 and HO-1, Aging (Albany NY) 12 (2020) 12943–12959.
[69] D.C. Fuhrmann, A. Mondorf, J. Beifuß, M. Jung, B. Brüne, Hypoxia inhibits ferritinophagy, increases mitochondrial ferritin, and protects from ferroptosis, Redox Biol. 36 (2020), 101670.
[70] W. Hou, Y.C. Xie, X.X. Song, X.F. Sun, M.T. Lotze, H.J. Zeh, R. Kang, D.L. Tang, Autophagy promotes ferroptosis by degradation of ferritin, Autophagy 12 (2016) 1425–1428.
[71] H.Y. Zhu, Q.T. Chen, Y. Zhang, L.L. Zhao, Glutathione s-transferase zeta 1 alters the HMGB1/GPX4 axis to drive ferroptosis in bladder cancer cells, Hum. Exp. Toxicol. 42 (2023), 1538540352.
[72] W. Han, L.Y. Zhu, E. Jiang, J. Wang, S.P. Chen, L.Z. Bao, Y. Zhao, A. Xu, Z.L. Yu, L. J. Wu, Elevated sodium chloride concentrations enhance the bystander effects induced by low dose alpha-particle irradiation, Mutat. Res./Fund. Mol. M. 624 (2007) 124–131.
[73] J.Z. Wu, B.H. Ye, L. Wang, L.N. Ji, J.Y. Zhou, R.H. Li, Z.Y. Zhou, Bis(2,2′-bipyridine) ruthenium(II) Complexes with Imidazo[4,5-F][1,10]-phenanthroline or 2-Phenylimidazo[4,5-F][1,10]phenanthroline, Journal of the Chemical Society, Dalton Trans., 1997, pp. 1395–1402.
[74] W. Paw, R. Eisenberg, Synthesis, characterization, and spectroscopy of dipyridocatecholate complexes of platinum, Inorg. Chem. 36 (1997) 2287–2293.
[75] S. Sprouse, K.A. King, P.J. Spellane, R.J. Watts, Photophysical effects of metal-carbon bonds in ortho-metalated complexes of Ir(III) and Rh(III), J. Am. Chem. Soc. 106 (1984) 6647–6653.
[76] H. Nie, X.M. Liu, Q.X. Yang, X.D. Luo, Y. Zhao, S.Y. Zhang, Effect of hydrophile–lipophile balance of the linker in Gal/GalNAc ligands on high-affinity binding of galactosylated liposomes by the asialoglycoprotein receptor, Int. J. Pharm. 624 (2022), 121967.
[77] Y.C. Chen, W.L. Li, Y. Yang, R.T. Zhong, H.Y. Hu, C.X. Huang, J. Chen, L.J. Liang, Y.J. Liu, Significant increase of anticancer efficacy in vitro and in vivo of liposome entrapped ruthenium(ii) polypyridyl complexes, Eur. J. Med. Chem. 257 (2023), 115541.
[78] E. Baka, J.E.A. Comer, K. Takács-Novák, Study of equilibrium solubility measurement by saturation shake-flask method using hydrochlorothiazide as model compound, J. Pharm. Biomed. 46 (2008) 335–341.
[79] T. Mosmann, Rapid colorimetric assay for cellular growth and survival: application to proliferation and cytotoxicity assays, J. Immunol. Methods 65 (1983) 55–63.